Summer 2023

Magma Residence Times and Pre-Eruptive Processes as Determined by Diffusion Geospeedometry and Textural Analysis—Lascar Volcano, Chile

Bennett G. Van Horn
Missouri State University, bgv79s@MissouriState.edu

MAGMA RESIDENCE TIMES AND PRE-ERUPTIVE PROCESSES AS DETERMINED BY DIFFUSION GEOSPEEDOMETRY AND TEXTURAL ANALYSIS – LASCAR VOLCANO, CHILE

A Master's Thesis

Presented to

The Graduate College of

Missouri State University

In Partial Fulfillment

Of the Requirements for the Degree

Master of Science, Geography and Geology

By

Bennett Van Horn

August 2023

MAGMA RESIDENCE TIMES AND PRE-ERUPTIVE PROCESSES AS DETERMINED BY DIFFUSION GEOSPEEDOMETRY AND TEXTURAL ANALYSIS – LASCAR VOLCANO, CHILE

Geography, Geology, and Planning

Missouri State University, August 2023

Master of Science

Bennett Van Horn

ABSTRACT

Petrographic textural analysis and geochemical microanalysis of plagioclase phenocrysts was conducted to model near-liquidus residence times and to gain further insight into processes that occurred within the magma chambers sourcing historical explosive eruptions at Láscar Volcano (NE Chile). Plagioclase crystals were analyzed from representative samples of Stages II (Soncor ignimbrite), III (Tumbres scoria deposit), and IV (Talabre lava, 1993 Plinian eruption). I used laser ablation-inductively coupled plasma mass spectrometry, which was combined with previously collected electron microprobe analyses and electron backscatter images to build a representative dataset of major- and trace element contents, as well as the zoning patterns and petrographic textures present. Analyzed phenocrysts can be grouped into five distinct populations, all of which record a major compositional change, evidenced by a section of reverse zoning and often resorbed zones, between the core and the mantle. A majority of the plagioclase also exhibit low-amplitude oscillatory zoning near the rim of the crystal. These textures have been interpreted as the result of a major magma mixing event that occurs once per stage, followed by smaller-scale fluctuations of conditions within the magma chamber. Major- and trace- element contents of plagioclase phenocrysts from Stages III and IV have also been modeled by diffusion geospeedometry using Python script published by Lubbers *et al.* (2022) to obtain paired Sr-Mg near-liquidus residence times. These models reveal that plagioclase resides in a warm and eruptible state, at the decadal-to-centennial scale, beneath Láscar prior to eruption. The average timescale has shortened through time, suggesting an increasing rate of small-volume injections of primitive magma, as proposed for Parinacota's Young Cone; aligning with predictions of relatively short residence times via bulk rock geochemical analysis.

KEYWORDS: Láscar, plagioclase, diffusion, geospeedometry, magma mixing, residence times, Python coding language, petrographic textures

MAGMA RESIDENCE TIMES AND PRE-ERUPTIVE PROCESSES AS DETERMINED BY DIFFUSION GEOSPEEDOMETRY AND TEXTURAL ANALYSIS – LASCAR VOLCANO, CHILE

By

Bennett Van Horn

A Master's Thesis
Submitted to the Graduate College
Of Missouri State University
In Partial Fulfillment of the Requirements
For the Degree of Master of Science, Geography and Geology

August 2023

Approved:

Gary Michelfelder, Ph.D., Thesis Committee Chair

Kevin Mickus, Ph.D., Committee Member

Toby Dogwiler, Ph.D., Committee Member

Julie Masterson, Ph.D., Dean of the Graduate College

ACKNOWLEDGEMENTS

There are several people and organizations that I would like to thank for their support during my graduate studies. First, I would like to thank the Missouri Space Grant Consortium, National Science Foundation, and Missouri State Graduate College for providing the funding that made this research possible. Much credit can be given to Dr. Gary Michelfelder, my primary research advisor, for the support and guidance that he was provided throughout the entirety of the project. I would also like to thank Dr. Kevin Mickus and Dr. Toby Dogwiler for serving on my committee. Further thanks are extended to Dr. Barry Shaulis for assistance with trace element analysis on the LA-ICPMS at the University of Arkansas, and to Kenny Horkley for assisting with the Electron Microprobe at the University of Iowa. I would also like to thank the following graduate students for their support throughout my graduate experience at Missouri State University: Cesar Bucheli-Olaya, Nathan Lenhard, Sarah Rasor, Chris Willingham, Drew Laviada-Garmon, Kasey Buckley, and Loren Bohannon.

TABLE OF CONTENTS

Introduction	Page 1
Geologic Background	Page 4
Andean Central Volcanic Zone	Page 4
Geology of Láscar Volcano	Page 5
Methods	Page 11
Bulk Rock Geochemistry	Page 11
Electron Probe Microanalysis	Page 12
Laser Ablation ICP-MS	Page 13
Results	Page 15
Petrology	Page 15
Plagioclase Petrographic Textures	Page 16
Whole Rock Major and Trace Element Geochemistry	Page 17
Plagioclase Major and Trace Element Geochemistry	Page 18
Discussion	Page 21
Plagioclase Textural Analysis & Crystal Stratigraphy	Page 21
Sr-Mg Diffusion Chronometry	Page 27
Conclusions	Page 34
References	Page 36
Appendices	Page 57
Appendix I. Plagioclase Major Element Spot Analyses	Page 57
Appendix II. Plagioclase Trace Element Spot Analyses	Page 57
Appendix III. Plagioclase Trace Element Line Transects	Page 57
Appendix IV. Sr-Mg Diffusion Models & Metadata	Page 57

LIST OF TABLES

Table 1. Normalized Whole Rock Major Element Data (Weight %) Page 43

Table 2. Unnormalized Whole Rock Trace Element Data (ppm) Page 44

Table 3. Individual Results of Sr-Mg Diffusion Modeling Page 45

LIST OF FIGURES

Figure 1. Location map of Láscar Volcano Page 46

Figure 2. Total alkali versus silica & major element bivariate diagrams Page 47

Figure 3: Plagioclase textural populations Page 48

Figure 4. Whole rock trace element variation diagrams Page 49

Figure 5. Bulk whole rock rare earth element diagram Page 50

Figure 6. Whole rock trace element variation diagrams of selected trace element ratios Page 51

Figure 7. Trace element variation diagrams of selected plagioclase major element compositions Page 52

Figure 8. Trace element variation diagrams of plagioclase spot analyses Page 53

Figure 9. Example plagioclase phenocryst core-to-rim transects and backscattered image Page 54

Figure 10. Rare earth element diagrams of plagioclase spot analyses Page 55

Figure 11. Sr and Mg diffusion age summary Page 56

INTRODUCTION

Láscar Volcano is often considered the most active volcanic center in the Andean Central Volcanic Zone (CVZ; Matthews *et al.*, 1999), with 32 Holocene eruptive periods (Smithsonian, 2013), and the largest recorded eruption (VEI 4) occurring in April 1993 (Déruelle *et al.*, 1996; Gardeweg *et al.*, 1998). The modern surficial expression of the volcanic center is of a dormant western edifice and an active eastern edifice composed of three overlapping craters formed through long-term cyclic activity expressed through dome growth, degassing, and subsidence of the dome and crater floor (Matthews *et al.*, 1999; de Zeeuw-van Dalfsen *et al*., 2016). Láscar provides the opportunity to study a volcanic system unique due to its immature nature, proclivity for explosive cyclic eruptions, and location atop 60-70 km of continental crust (Allmendinger *et al*., 1997). Additionally, this volcanic center falls within the boundaries of the Altiplano-Puna Volcanic Complex but is located outside the proposed extent of the Altiplano-Puna Magma Body from geophysical studies (Zandt *et al*., 2003; Ward *et al*., 2014; Pritchard *et al*., 2018).

Previous studies on Láscar have described the volcano's stratigraphy and petrology of individual eruptions (Matthews *et al*., 1994; Matthews *et al*., 1997) as well as detailing the evolution and geometry of the magma chamber (Gardeweg *et al*., 1998; Matthews *et al*.,1999). However, it is unclear the duration that magma resides beneath the volcano prior to eruption. The purpose of this study is to use plagioclase to investigate this magmatic process as it is a ubiquitous igneous mineral in all Láscar eruptive products that crystalizes over a wide range of temperatures and compositions, has identifiable compositional zoning, and can grow large enough have the spatial resolution to accommodate analyses via microspatial techniques (Costa *et al*., 2003).

In recent years, Láscar Volcano has been the focus of an increasing number of geophysical (Hellweg, 2003; Pritchard *et al*., 2014), LiDAR and remote sensing (Francis & Rothery, 1987; Francis *et al*., 1989; Oppenheimer *et al*., 1993; Wooster, 2001; Pavez *et al*., 2006; Jay *et al.*, 2013; Pritchard *et al.*, 2014; González *et al.*, 2015), fumarole gas chemistry (Tassi *et al.*, 2008; Gaete *et al*., 2020), isotope geochemistry (Harmon *et al.*, 1984; Sainlot *et al.*, 2020), pyroclastic flow rheology (Sparks *et al.*, 1997; Jessop *et al*., 2012), and architecture of the magma plumbing system (Robidoux *et al.*, 2020; Stearn, 2020) studies, but the residence times of plagioclase crystals at near-liquidus (warm and eruptible) conditions within the magma chamber have yet to be elucidated. This gap in understanding of the plumbing system inhibits understanding of the cyclicity of Láscar's eruptive cycle. Additionally, crystal residence times record the approximate interval as the eruptive frequency of the volcano from which they are sourced (Costa *et al*., 2020). At Láscar, many rocks show evidence of magma mixing, with disequilibrium phenocryst assemblages and compositionally banded pumices and lava (Gardeweg *et al*., 1998). This evidence of open-system processes solidifies Láscar as an excellent locality for the study of residence times through paired Mg-Sr diffusion plagioclase geospeedometry due to the existence of necessary compositional gradients.

In this study I present new major and trace element, whole rock and plagioclase geochemical data for five eruptive units spanning three eruptive stages of Láscar's history: the Soncor Ignimbrite, Talabre lava, Tumbres pyroclastic deposit, and the April 1993 plinian eruption (banded and non-banded end-members). These data was utilized via open-source Python diffusion script published by Lubbers *et al.* (2022) to obtain paired Mg-Sr diffusion models to determine near-liquidus residence times for plagioclase phenocrysts from Stages III and IV of Láscar's eruptive history. Modeled residence times are combined with textural

analyses of analyzed plagioclase phenocrysts allowing insight into the dynamics within the magma chamber, which suggests the existence of a mixing event that occurred prior to the initiation of each major eruption that marked the end of each stage within the volcano's history. The modeled residence times occur on a relatively short decadal to centennial scale and exhibit a trend that becomes progressively younger through time, which suggests that Láscar exhibits a unique state within the CVZ whose activity is similar to that of Parinacota's Young Cone as suggested by Ginibre & Wörner (2007) and Wörner *et al.* (2018). These results agree with the relatively short residence times as predicted via bulk rock geochemical analysis by Robidoux *et al.* (2020).

GEOLOGIC BACKGROUND

Andean Central Volcanic Zone

The Andean Cordillera is often considered the classic example of a modern Cordilleran-type orogen, formed by the long-term subduction of the oceanic Nazca plate beneath continental lithosphere (Manami *et al*., 2008; Michelfelder *et al*., 2013). Modern subduction between the South American and Nazca plates occurs with an azimuth of N79°E at the rate of ~63 mm/yr for the central Andean margin, with a peak rate of more than 150 mm/yr between 25 and 20 Ma (Kendrick *et al*., 2003; Manami *et al*., 2008). Within the cordillera, active volcanoes are present where the angle of subduction is relatively steep (>25°), defining four zones of volcanism: the Northern, Central, Southern, and Austral Volcanic Zones (Allmendinger *et al*., 1997; Mattioli *et al.* 2006). These zones are separated by sections where the subduction angle shallows (<10°) and volcanic activity quiesces (Mattioli *et al.*, 2006).

The Central Volcanic Zone (CVZ) is characterized by the thickest continental crust of any subduction zone on Earth (70+ km in the Altiplano and 60-70 km in the Puna Plateau; Allmendinger *et al*., 1997; Mamani *et al*., 2010), and as a multitude of incredibly well-preserved volcanic centers resulting from its location within the Earth's climate belts (de Silva, 1989; Montgomery *et al*., 2001). The accumulation of such an immense volume of continental crust has been attributed to the actions of crustal shortening, delamination, and magmatic addition through its geologic history, as well as the recent steepening of the subducting slab, though the contributions and timings of each process are still widely debated (Allmendinger *et al*., 1997; Manami *et al*., 2010; Michelfelder *et al*., 2013). Regionally, the Miocene to Quaternary volcanic centers of the western Altiplano and Cordillera, whose ages range from, vary compositionally

from andesitic stratocones to dacitic dome complexes and extensive caldera complexes with associated large-volume ignimbrite deposits (de Silva, 1989; Calder *et al.,* 2000).

Geology of Láscar Volcano

Láscar Volcano (5592 m; 23° 22’ S, 67° 44’ W) is the most active volcanic center in the northern Chilean Andes. The volcanic center is located in the Andean Central Volcanic Zone (CVZ) in a physiographic domain known as the Cordillera de los Andes, which is bordered to the east by the Andean plateau (Altiplano), and to the west by the Salar de Atacama (Figure 1). The basement rock beneath Láscar is composed Devonian to Early Carboniferous sandstones with distinctive quartzite (Lila Formation), Permian volcanic rocks and granites containing epidote and chlorite (Cas Formation), and volcanic Permo-Triassic rocks (Peine Strata and Cerro Negro Strata; Gardeweg *et al*., 1998 & *references therein*; Calder *et al*., 2000). The volcanic edifice itself has been constructed on a ridge of dacite domes referred to as the Cerro Corona and Cerro de Saltar dome complexes, which extends north and south of Láscar along a major tectonic lineament (the Miscanti line; Gardeweg *et al.*, 1998; Calder *et al*., 2000). Locally, Láscar is adjacent to two other major volcanic centers: Tumisa Volcano and Volcan Aguas Calientes (Gardeweg *et al*., 1998 & *references therein*).

The structure of Láscar Volcano is elongate, exhibiting an east/northeast-west/southwest trend with six overlapping summit craters, the central crater being the locus of the most recent activity (Global Volcanism Program, 1993; Global Volcanism Program, 2017; Global Volcanism Program, 2022). Over its eruptive history, the active crater of the volcano has migrated westward from the eastern side of the edifice, before reversing back to the eastern side at ~ 7 ka, placing the active craters on the site of the original stratocone (Calder *et al*., 2000). Eruptive products

from Láscar Volcano are primarily ignimbrite flows and lavas, which are often accompanied by scoria and volcanic bombs (Matthews *et al*., 1994; Gardeweg *et al*., 1998; Calder *et al*., 2000). Major rock types of the volcanic center include porphyritic andesites and dacites, with plagioclase as the dominant phenocrysts within the mineral assemblage (Matthews *et al*., 1994). Mafic andesites contain olivine, orthopyroxene and clinopyroxene, whereas silicic andesites and dacites contain two-pyroxenes alongside hornblende and biotite in the most evolved units (Gardeweg *et al.* 1998). Current activity at Láscar is composed of persistent fumaroles (Tassi *et al*., 2008), a thermal anomaly detectable by satellite (Oppenheimer *et al*., 1993; Wooster, 2001; Jay *et al*., 2013; Pritchard *et al*., 2014; González *et al*., 2015; Global Volcanism Program, 2017), and regularly occurring small-scale seismic events (Hellweg, 2003; Pritchard *et al*., 2014; Global Volcanism Program, 2022). Gardeweg *et al.* (1998) divided the evolution of the volcano into four distinct stages, described in further detail below.

Stage I. Activity at Láscar began with the building of an andesitic stratocone (Láscar I), with the oldest eruptive products recorded consisting of blocky pyroxene andesite lavas. These Stage I lavas are typically microporphyritic, strongly plagioclase phyric and glassy with zeolites commonly found infilling vesicles (Gardeweg *et al*., 1998). Activity at Láscar I culminated with the eruption of three coarse-grained andesitic pyroclastic flow eruptions: the Saltar deposit (167±9 ka), and the Lower and Upper Chaile deposits (167±9; Aguilera Barraza, 2018). The Saltar deposit consists of a very coarse-grained pyroclastic flow deposit primarily composed of large brick red cauliform andesite bombs, set within a poorly-sorted ashy scoriaceous matrix (Gardeweg *et al.*, 1998). The Saltar deposit has at least nine recorded flow units that have been observed within the thickest sections of the deposit, and degree of welding varies dependent on

its position along Láscar's flanks, with deposits north of the volcano being the most strongly welded (Gardeweg *et al.*, 1998).

The Upper and Lower Chaile deposits are similarly two coarse-grained andesitic pyroclastic flow deposits, with the Lower Chaile being more coarse-grained than the Saltar (Gardeweg *et al*., 1998). The deposit is composed of abundant dense cauliform rounded pyroclastic bombs in a poorly-sorted ashy matrix, having a minor component of bombs of agglutinate spatter and welded lava breccia (Gardeweg *et al.*, 1998). The Upper Chaile is present within topographic lows cut within the Lower Chaile deposit, and is composed of a dark grey andesitic scoria and is distinguished from the Lower Chaile by the presence of biotite-bearing dacite xenoliths (Matthews *et al*., 1994; Gardeweg *et al*., 1998).

Stage II. The transition to Stage II is marked by a shift in activity to the west and the formation of a silicic andesite and dacitic lava dome complex (Gardeweg *et al*., 1998). Two eruptive products of note from Stage II include the Piedras Grandes unit (>26.5 ka) and the Soncor Ignimbrite (26.5 ka; Gardeweg *et al*., 1998). The Piedras Grandes is defined as a pink-to-grey ignimbrite deposit, and is composed of silicic hornblende andesite containing minor basaltic andesite bands and inclusions (Gardeweg *et al.*, 1998; Matthews *et al.*, 1999). This unit has been interpreted as being formed by hot avalanche deposits resulting from lava dome instability (Gardeweg *et al*., 1998 & *references therein*; Matthews *et al.*, 1999). A second component of the Piedras Grandes can be found as thin layers of fluvial deposits, whose emplacement has been interpreted as the result of a catastropic flood event produced by glacier bursts (jokulhaulps; Gardeweg *et al.*, 1998).

Overlying the Piedras Grandes unit is the Soncor Ignimbrite, which is composed of multiple flows, and is the most voluminous pyroclastic deposit of Láscar's eruptive history

(minimum eruptive volume of 15 km^3). The ignimbrite is composed of a plinian pumice deposit and overlying thick pumice- and lithic-rich ignimbrite fans (Gardeweg *et al*., 1998; Matthews *et al*., 1999). Pumice is largely composed of compositionally heterogeneous white two-pyroxene andesite to dacite pumice that ranges in color depending on SiO_2 content, the uppermost 2 m consisting of a prominent compositionally-banded pumice (Matthews *et al*., 1999). The main juvenile component of the Soncor Ignimbrite is a white dacitic pumice, with the uppermost flow units of pumice and scoria being compositionally zoned, with diverse compositions ranging from basaltic to silicic andesite (Gardeweg *et al.*, 1998; Matthews *et al.*, 1999). The plinian deposit and the ignimbrite are both normally zoned, with a compositional reversal found at the boundary between, a pattern described in the literature as "double zoning" (Gardeweg *et al.*, 1998; Matthews *et al.*, 1999).

Stage III. With Stage III, activity persisted on the western side of Láscar, with the construction of an andesitic-dacitic stratocone over the location of the Soncor vent (Gardeweg *et al.*, 1998, Matthews *et al*., 1999). The composition of lavas erupted during this stage are silicic andesites to dacites which include the Capricorn lava, as well as at least one additional scoria flow (Gardeweg *et al.*, 1998; Matthews *et al*., 1999). The exact timing of the construction of the Stage III stratocone is still unclear, but is thought to have occurred between 19.2 and 9.2 ka in the period between geomorphological events that occurred at the terminus of Stage II, and prior to the Talabre lava attributed to Stage IV (Gardeweg *et al.*, 1998; Matthews *et al.*, 1999). The culmination of Stage III was marked by the Tumbres eruption (9.3-9.1 ka) which formed a thin pumice fall deposit alongside fans of red scoria and andesitic cream-colored pyroclasts (Gardeweg *et al.*, 1998; Matthews *et al.*, 1999). The deposits are scoria-rich with moderate vesicularity, set within a matrix of dark grey to reddish ash. Banded scoria exhibiting white

dacitic streaks of pumice are also occasionally present (Gardeweg *et al*., 1998). Juvenile clasts associated with this eruption consist of phyric two-pyroxene andesites and olivine-clinopyroxene basaltic andesites, with associated lithic clasts including oxidized red and orange lava pyromorphic xenoliths that include quartzites and calcsilicates (Matthews *et al.*, 1996; Gardeweg *et al.*, 1998).

Stage IV. Following the Tumbres eruption, activity shifted back to the eastern vents of the complex, forming the three modern summit craters (Oppenheimer *et al.*, 1993; Jay *et al*., 2013; González *et al.*, 2015; de Zeeuw-van Dalfsen *et al*., 2017). Activity within Stage IV continued with the formation of craters via collapse alternating with infilling by andesitic lava and volcanic ejecta (Gardeweg *et al.*, 1998). The resulting andesitic Talabre lava (7.1 ka) formed due to the overflow of the craters and consists of a blocky and glassy two-pyroxene porphyritic andesite containing oxyhornblende (Gardeweg *et al.*, 1998). Historic activity can be dated back to 1848 and largely involves the cyclic activity of lava dome growth, subsidence, and degassing accompanied by occasional volcanian to plinian eruptions (Gardeweg *et al.*, 1998; Matthews *et al*., 1997, Matthews *et al.*, 1999). This cyclic behavior culminated in the April 1993 plinian eruption, the largest in record sinces the Tumbres eruption (Déruelle *et al.*, 1996; Gardeweg *et al*., 1998).

April 1993 Plinian Eruption. The largest historical eruption recorded at Láscar Volcano began at 10:00 pm local time on April 18, 1993. Láscar's primarily phreatic activity was interrupted by a large explosion that expelled incandescent material 20-22 km above the summit (Global Volcanism Program, 1993). The collapse of the eruption columns resulted in the creation of light-colored pumice flows that descended both southwards and northwards through the Tumbres Canyon, with the furthest flow reaching 8.5 km to the northwest of the summit (Global

Volcanism Program, 1993; Déruelle *et al.*, 1996; Gardeweg *et al.*, 1998; Global Volcanism Program, 2017). The total erupted mass has been estimated at around 1,012 kg with a volcanic explosivity index (VEI) of 4 for the eruption (Déruelle *et al*., 1996).

Déruelle *et al*. (1996) described the composition of the dome lava that was emplaced following the eruption as porphyritic andesite containing olivine mantled with orthopyroxene as well as abundant augite and enstatite phenocrysts, with scarcer unstable phenocrysts of augite and enstatite. The pumice erupted is dacitic in composition, with phenocrysts of plagioclase, enstatite, augite, phlogopite, magnetite, and ilmenite (Déruelle *et al*., 1996). Of note is the absence of hornblende, as it is both commonly observed in Láscar lavas and is often found in dacites alongside augite, enstatite, and biotite (Déruelle *et al*., 1996). Post 1993, intermittent activity has been recorded at Láscar with the occurrence of 13 minor eruptions, largely phreatic in nature, the most recent of which began in early December 2020 and has continued into February 2023 and is accompanied by persistent degassing from vents in the summit crater (de Zeeuw-van Dalfsen *et al*., 2017; Global Volcanism Program, 2022; Global Volcanism Program, 2023).

METHODS

Bulk Rock Geochemistry

Nine samples composing five historical eruptions from Láscar Volcano (Piedras Grandes (>26.5 ka), Soncor Ignimbrite (26.5 ka), Tumbres eruption (9.3 ka), Tumbres-Talabre lava (7.1 ka), and April 1993 eruption) were selected for bulk rock geochemical analysis. Samples were analyzed at Washington State University for both major (SiO_2, TiO_2, Al_2O_3, FeO, MnO, CaO, Na_2O, K_2O, P_2O_5) and trace element (La, Ce, Pr, Nd, Sm, Eu, Gd, Tb, Dy, Ho, Er, Tm, Yb, Lu, Ba, Th, Nb, Y, Hf, Ta, U, Pb, Rb, Cs, Sr, Sc, Zr, V, Cr, Ni, Cu, Zn, Ga) compositions. Major elements, and their corresponding uncertainties were characterized using a ThermoARL AdvantXP XRF and the method of Johnson *et al*. (1999). Bulk rock major and trace element concentrations can be found in Supplementary Data Tables 1 and 2.

Five samples composing four historical eruptions from Láscar Volcano (Soncor Ignimbrite (26.5 ka), Tumbres eruption (9.3 ka), Tumbres-Talabre lava (7.1 ka), and April 1993 eruption) were selected for bulk rock trace element analysis by inductively-coupled plasma mass spectrometry (ICP-MS) at Missouri State University (La, Ce, Pr, Nd, Sm, Eu, Gd, Tb, Dy, Ho, Er, Tm, Yb, Lu, Ba, Th, Nb, Y, Hf, Ta, U, Pb, Rb, Cs, Sr, Sc, Zr). Trace element contents including the rare earth elements (REEs) and their uncertainties were determined using an Agilent 7900 quadrupole ICP-MS. Samples were ground to a powder using a steel jaw crusher and tungsten carbide planetary ball mill. Digestion details and analytical procedures are like those described in Liu *et al*. (2008). An aliquot of 50 mg of sample was dissolved in a sequence of acid digestions. Initial digestion was in 3:3 ml solution of HF and HNO_3 at 210°C for 24 hours in a closed Teflon beaker on a hot plate. When the solids were completely dissolved, the acid

was evaporated, and the process was repeated for two additional rounds of digestion. The second digestion contained 3 ml of HNO_3 and the third with 3 ml of HCl. A final round of digestion contained 3 ml of HNO_3 in an enclosed beaker for 12 hours. One milliliter of H_3BO_3 was added to the sample then diluted to 100 grams. An aliquot of the digested solution of 15 ml was analyzed by ICP-MS and corrected for spectral interferences. Three USGS reference materials were used to calibrate the analysis and correct for analytical drift: STM-2, AGV-2, and RGM-2. Further quality control was assured by co-analyzing the reference materials with the unknowns. All reference material analyses overlap with certified values at 2σ. The precision of these analyses was better than 5%.

Electron Probe Microanalysis

Major element oxides (Na_2O, SiO_2, Al_2O_3, FeO, CaO, K_2O, MgO, TiO_2) spot analyses and backscattered electron (BSE) images of plagioclase phenocrysts were conducted on the JEOL JXA-8230 Superprobe (EPMA) at the University of Iowa at an accelerating voltage of 15 kV, a beam current of 20 nA, and a working distance of 11.1 nm. Calibration used Astimex Plagioclase and an internal microcline standard from the University of Iowa. Data was collected as a series of core-to-rim spot transects, with the number of spot analyses dependent on phenocryst size, expressed zoning, and the number and size of zones present as one spot analysis was taken per distinct rim composition observed. Uncertainties were calculated by repeated measurement of standard reference values. Average measured values, accepted values, and their uncertainties can be found within Supplementary Data in Appendix I.

Laser Ablation ICP-MS

Trace element analyses of pumice glass, and plagioclase and pyroxene phenocrysts were conducted using an ESL NWR 193 laser ablation system connected to a ThermoFisher iCAP-RQ ICP-MS at the University of Arkansas's Trace Element and Radiogenic Isotope Laboratory. Previously collected BSE images of plagioclase and pyroxene phenocrysts were used to identify mineral textures and characterize zoning for the purpose of selecting phenocrysts for analysis. Analyses consisted of the following trace elements: plagioclase – ^{7}Li, ^{24}Mg, ^{45}Sc, ^{48}Ti, ^{52}Cr, ^{57}Fe, ^{66}Zn, ^{85}Rb, ^{88}Sr, ^{89}Y, ^{90}Zr, ^{93}Nb, ^{133}Cs, ^{137}Ba, ^{178}Hf, ^{208}Pb, ^{232}Th, ^{238}U, and REEs; pyroxene – ^{27}Al, ^{31}P, ^{43}Ca, ^{45}Sc, ^{47}Ti, ^{51}V, ^{52}Cr, ^{55}Mn, ^{60}Ni, ^{88}Sr, ^{89}Y, ^{90}Zr, ^{93}Nb, ^{178}Hf, ^{181}Ta, ^{232}Th, ^{238}U, and REEs; pumice glass – ^{7}Li, ^{24}Mg, ^{29}Si, ^{45}Sc, ^{47}Ti, ^{52}Cr, ^{57}Fe, ^{66}Zn, ^{85}Rb, ^{88}Sr, ^{89}Y, ^{90}Zr, ^{93}Nb, ^{133}Cs, ^{137}Ba, ^{178}Hf, ^{208}Pb, ^{232}Th, ^{238}U, and REEs. Significantly elevated values for Mg, Ti, and Fe are attributed to the ablation of unseen microlites during analysis and have been excluded from further consideration. Analyses of plagioclase were conducted as core-to-rim line transects paired with a line of 3 to 4 spot analyses spaced adjacent to the length of the transect to increase analytical precision. Transects were preferentially oriented along crystallographic axes and plotted to avoid disequilibrium textures and cracks present in the exposed surface. A spot analysis of pumice glass was taken proximal to each plagioclase phenocrysts of interest. Due to the small size of available pyroxene phenocrysts, analyses were conducted as a pairing of spot analyses: one centered in the core of the phenocryst and the other placed near the rim. Approximately 10 plagioclase and 5 pyroxene phenocrysts were analyzed per sample, with up to two transects analyzed on each plagioclase, dependent on the size of the phenocryst. Analyses were programmed with a spot size of 50 μm, pulse rate of 10 Hz, and an analysis time of 20 seconds per spot. The laser was set to 50% power (or 3 J/cm^2) for all analyses and moved at a

rate of 10 μm/s for the line transect scans. Reference materials and glasses, NIST610 and NIST612 (Jochum *et al*., 2011), were used as primary calibration standards. In total, 50 plagioclase transects across 34 phenocrysts were gathered. Collected data was reduced in the Iolite 4 software (Woodhead *et al*., 2007; Paton *et al*., 2011) to remove outliers outside of 2σ error. REEs were normalized to chondritic values as suggested by McDonough & Sun (1995). Analyses suggest precision for trace elements measurements in all materials are better than 5%. The complete dataset of all major and trace element plagioclase compositions and standard compositions are included in Appendices II and III.

RESULTS

This study presents new data from six previously studied pumice samples from Láscar Volcano. Data was combined with those from previous studies conducted upon Láscar (Matthews *et al.*, 1999; Robidoux *et al.*, 2020; Stearn, 2020). Samples utilized in this study represent stages II, III, and IV of Láscar's eruptive history. Stage II is represented by sample LASC-P01 from the Soncor eruption. Stage III is LASC-P02, a pumice from the Tumbres eruption. Samples from Stage IV include LASC-25T-01, from the Talabres lava, as well as LASC-P03, LASC-P03A, and LASC-P03B, the light dacitic end member of the bimodal pumice from the April 1993 plinian eruption, the banded intermediate member, and the darker mafic endmember from the same April 1993 eruption, respectively.

Petrology

The petrology of samples used here were described in detail by Stearn (2020). Volcanic rocks from Láscar are porphyritic to microporphyritic andesites and dacites (Figure 2) with a phenocryst assemblage of plagioclase, two-pyroxenes (the prevalence of ortho- or clinopyroxene varying by eruption), and hornblende, listed in order of descending abundance. Percentage of phenocrysts represented in thin section vary from 28-47% (Stearn, 2020), with pumice from the Soncor Ignimbrite being less crystal-rich than pumices from either Stage III or IV. Plagioclase is the most dominant phenocryst phase, with pyroxenes becoming increasingly more common in the more mafic samples. Stearn (2020) described plagioclase groundmass as bladed microlites as well as being present as subhedral and tabular phenocrysts (An_{35-86}). The plagioclase phenocrysts present often display complex combinations of multiple textures and zoning patterns, with

normal zoning, reverse zoning, oscillatory zoning, and patchy zoning as the main zoning patterns observed (Figure 3).

Plagioclase Petrographic Textures

Plagioclase textures are illustrated in a backscattered electron (BSE) image in Figure 3. For the purposes of this study, the "core" of a phenocryst is the innermost region, the "rim" being the outermost zone in contact with the surrounding glass, and the area in-between referred to as the "mantle." Across all samples, plagioclase phenocrysts can be classified into six distinct populations, based on petrographic textures present (Figure 3). Type I plagioclase are unzoned and exhibit no other distinct petrographic textures. Type IIa have no coarse or fine sieving in the core or rim, and are oscillatory or normally zoned, with widespread pockets of resorption that have removed portions of zonation. Type IIb are similar to that of Type IIa, but lack evident resorption surfaces. Type III have a core that is almost entirely resorbed, with normal to oscillatory zoning through the mantle to the rim. Type IV contain mineral inclusions within a coarsely-sieved core, with minor localized resorption and oscillatory to normal zoning within the mantle and rim of the phenocryst. Type V phenocrysts have coarse sieving within the core, with fine sieving textures near the rim and osillatory zoning within the intermediary mantle.

In Stage II, only Type IIa plagioclase are present. For Stage III, Types IIb, III, IV, and V can be found. Stage IV contains Types I, IIa, III, and IV. The presence of textural populations has fluctuated throughout Láscar history with no plagioclase textural population being present in samples from all three stages. Type IIa is present in Stage II, but does not appear again until eruptions from Stage IV. Type I is found only in Stage IV eruptions, whereas Type IIb and V are

only present in eruptions from Stage III. Populations that are shared betweens stages are Type IIa (Stage I and IV), as well as Types III and IV (Stage III and Stage IV).

Whole Rock Major and Trace Element Geochemistry

Major and trace element data for Láscar samples are illustrated in Figure 2 and Figures 4-6, and presented in Tables 1 and 2. Pumice are high-K calc-alkalic andesites and dacites ranging in SiO_2 from 58-61%. Linear trends are present within the data for most of the major elements, with previous data from Matthews *et al.* (1999) spanning the greatest range of SiO_2 and exhibiting the most geochemical variation. With increasing SiO_2, K_2O (1.58-2.04%) increases, with samples from the April 1993 eruption having the lowest SiO_2 and K_2O, with the Soncor Ignimbrite, and the Piedras Grandes lavas listed in order of increasing K_2O (Figure 2). Conversely, TiO_2 (0.72-0.85%), FeO (5.7-6.49%), CaO (6.02-7.09%), and MgO (3.43-4.8%), decreases with increasing SiO_2 (Figure 2). No distinct relationship is observed between SiO_2 and Na_2O (3.23-3.78%), instead forming a disperse cloud, with samples from the Piedras Grandes lava exhibiting the highest Na_2O, and samples from April 1993 eruption and the Soncor ignimbrite plotting in the same space (Figure 2).

Linear trends are also observed in the collected whole rock trace element data. Barium (372-434 ppm), Pb (11-15 ppm), and Rb (56-78 ppm) concentrations have a positive correlation with increasing SiO_2 content (Figure 4), whereas, Sr (450-577 ppm) concentrations have no discerable relationship with increasing SiO_2 (Figure 4). Increasing Eu*, relates to a negligible negative linear relationship in the Eu/Eu* value, progressing from the April 1993 eruption, the Soncor Ignimbrite, and the Piedras Grandes lavas (Figure 4). Sr/Y ratio versus Y, shows a tight cluster centered around ~20 ppm Y and a Sr/Y ratio of ~25 (Figure 4). A distinct negative linear

trend is present when the Rb/Sr ratio versus Sr (Figure 4), with all samples falling within the high Sr, low Rb/Sr segment of the Piedras Grandes and Soncor samples analyzed by Matthews *et al.* (1999). With increasing Sm concentration, La concentration becomes more restricted across all samples (Figure 4). Láscar pumice is enriched in light rare earth elements (LREEs) compared to middle (MREEs) and heavy rare earth elements (HREEs; Figure 5). Additionally, pumice are more constrained for LREEs, with marginally more variation in the MREEs and HREEs. A negative relationship exists for La/Yb_N ratio versus Yb_N (Figure 6). Furthermore, a positive linear relationship exists for Dy/Dy* ratio vs. Dy/Yb_N, with analyses from the Piedras Grandes Lavas having both the lowest and highest Dy/Dy* and Dy/Yb_N values (Figure 6).

Plagioclase Major and Trace Element Geochemistry

Representative plagioclase major and trace element chemistry is presented in Figure 7-10, and the full dataset of plagioclase phenocryst major element chemistry is included in Appendices I, II, and III. For all samples, with increasing An_x, no discernable relationship with TiO_2 (BDL-0.81 wt%), FeO (0.21-5.35 wt%), or MgO (0.009-5.50 wt%) is observed. The Talabre lava samples express the greatest major element variation of the eruptions included in this study. Across all samples, within individual plagioclase phenocrysts,TiO_2 wt%, FeO wt%, MgO wt%, and An_x (anorthite content) fluctuate from the core, through the mantle, and to the rim of each phenocryst. Elevated or depleted values within the transects of TiO_2 wt%, FeO wt%, MgO wt%, or An_x are not isolated to the cores, mantles, or rims of each phenocryst, but appear to vary between individual plagioclase phenocrysts for all analyzed eruptions across all stages of Láscar's eruptive history.

Trace elements of interest in all samples create two linear trends (Figure 8). The upper trend is defined by the Tumbres eruption and Talabre lava, with the lower trend defined by the April 1993 banded pumice and Soncor Ignimbrite. Plagioclase contents vary significantly between individual phenocrysts and are not isolated to cores, mantles, or rims, but appear to fluctuate across each analyzed mineral (Figure 9). Spot analyses representing the Soncor Ignimbrite across all elements exhibit a horizontal linear trend, with no change in the element of interest: Mg (171.54-20323 ppm), Ti (67.03-19382 ppm), Sr (9.33-2060 ppm), Fe (1038.77-26322 ppm), Rb (0.22-111 ppm) with increasing Li (4.91-117 ppm) concentrations (Figure 8). Concentrations for the Soncor Ignimbrite generally decrease across the phenocryst for all elements, with highest values in the core, and decreasing through the mantle to the rim. The Tumbres eruption and Talabre lava exhibit the greatest variability, with no clear distinction between contents for the core, mantle, and rim for all elements of interest. Contents for the light and banded end-members of the April 1993 plinian eruption are the most constrained geochemically, and plot in very similar spaces, with analyses of the banded pumice having comparatively slightly elevated Li contents for a given trace element. A few cores and mantles from the April 1993 plinian eruption are also significantly enriched in Rb for a given Li content (Figure 8), separating these analyses from the rest of the values from the samples, which are tightly clustered.

Within individual crystals across all samples, two populations of crystals can be observed. The first population has stable Sr contents from core-to-rim, and variability in Mg along the transect (Figure 9). The second population has stable Sr and Mg contents from the core to the rim of the phenocrysts. These populations are not restricted to individual samples, but are present in transects from all samples analyzed samples. REE trends for plagioclase have greater

concentrations of LREEs than HREEs and positive Eu anomalies, with the exception of a few analyses that have either very minor or non-discernable Eu anomalies (Figure 10). The anomalous analyses with little variation in REE values are not attributed to the same plagioclase phenocryst, and primarily represent the core or mantle of their respective phenocryst. Within analyses from each eruption, LREEs and MREEs also appear to be far more constrained when compared for HREEs for all samples.

DISCUSSION

Plagioclase Textural Analysis and Crystal Stratigraphy

The zoning patterns of mineral phenocrysts are a valuable source of information that can be used to reconstruct the processes which have occurred in magmatic reservoirs and volcanic conduits (Costa *et al.*, 2008). Several studies have suggested the occurrence of multiple recharge events across several volcanic centers before eruption, with redistribution and dispersion of growing crystals throughout the magma chamber resulting in the recording of different environments and crystallization conditions within a single eruptive unit (Tepley *et al.*, 2000; Ginibre *et al.*, 2007). Minerals such as plagioclase, grow progressively outward in zones from the center—or core—of the phenocryst, the pattern of zoning and the presence of petrological textures can be interpreted to reconstruct the often tumultous history of individual phenocrysts from storage to eruption (Ginibre *et al*., 2002; Berlo *et al*., 2007; Shcherbakov *et al*., 2010; Renjith, 2014; Viccaro *et al*., 2016; Fabbro *et al*., 2017).

Shcherbakov *et al.* (2010) outlines commonly used terminology used to describe the main elements of plagioclase zoning. In simple terms, unzoned areas of of minerals are characterized by a constant composition. Normal zoning (Type I, II, III, IV) describes a change in composition that shifts from higher to lower anorthite content, progressing outward from the center of the phenocryst. Normal zoning reflects fractional crystallization of the magma body as the melt composition slowly evolves over time, gradually progressing from a more calcic to a more sodic composition (Ginibre *et al.*, 2007). Reverse zoning (Types II, III, IV, V) reflects increasing An content outwards from the center of the phenocryst and occurs when the outer portions of the phenocryst equilibrates with a melt of a more calcic composition than that of the core (Ginibre *et*

al., 2002). This reflects the occurrence of a mixing event between the magma hosting the phenocryst and often more primitive magma during the growth of the phenocryst. Such mixing can also be marked by the presence of resorption if there is an accompanying change in minor elements, such as Ca and Na (Ginibre *et al.*, 2007).

Oscillatory zoning (Types II, III, IV, V) is exhibited as thin zones of differing An content, with neighboring zones fluctuating by less than 2-3 mol% An. Oscillatory zoning can be interpreted as fluctuating external conditions resulting from a convecting magma chamber or repeated influxes of fresh magma into the magma chamber, and has been divided into two categories by Ginibre *et al.* (2002). Saw-tooth oscillation with resorption consists of repeated normally-zoned growth layers, which are separated by wavy boundaries and a sharp increase in An content. The boundary between individual zones has been interpreted as minor resorption events as only one growth layer is affected, potentially resulting from convection within the magma chamber (Ginibre *et al.*, 2002). Low-amplidude oscillations occur as repeated faint variations in composition with straight boundaries, occuring as the by-product of a kinetic effect at the crystal-melt boundary (Ginibre *et al*., 2002). Of interest to this study is oscillatory zoning expressed as low-amplitude oscillations, as minor resorption are not observed affecting individual growth layers.

Resorption surfaces (Types IIa, III, IV) are defined by evidence of intensive resorption such as tunnel dissolution, dusty zones, and embayed boundaries. Resorption within the plagioclase cores occurs as the composition of the phenocryst reacts in accordance with instability of the conditions of the magma chamber, with minor dissolution being interpreted as pressure and temperature related, whereas, significant dissolution is caused by changes in chemical composition of the melt (Ginibre *et al.*, 2002; 2007). Patchy zoning (sieving) is

represented by a sponge-like corroded calcic core that is filled and surrounded by a more sodic composition. Coarse-sieve morphology (Types IV, V) appears largely amoeboidal and frequently appears at the core of plagioclase, whereas, fine-sieves (Type V) are uniformly distributed within a single zone (Renjith, 2014). Coarse-sieve textures are interpreted to occur via dissolution by varying rate of adiabatic decompression of H_2O undersaturated magma, and contrast with more isolated fine-sieve textures that result from partial dissolution due to a reaction with a more Ca-rich melt (Renjith, 2014). A morphological texture present within the phenocrysts is synneusis, which results from a turbulent magmatic state-related convection, causing the drifting together and mutual attachment and subsequent growth of plagioclase phenocrysts (Renjith, 2014). Broken phenocrysts, as evidenced by cracks and fragmented edges, are attributed to the violent style of eruption present throughout Láscar's history (Déruelle *et al.*, 1996; Gardeweg *et al.*, 1998; Matthews *et al.*, 1999). A small number of plagioclase phenocrysts have also developed a swallow-tail, which can be attributed to rapid growth due to undercooling (Renjith, 2014).

Backscattered electron images (BSE) and chemical maps from analyzed plagioclase phenocrysts across all eruptions of interest show several common features, which divide the zoned plagioclase phenocrysts into two simplified populations. The first population exhibits a coarsely-sieved core (Figure 3), whereas the second population describes phenocrysts with small pockets of melt inclusions in the core, and often fine-sieve textures near the edge of the phenocryst. The cause for these sieving textures have been previously interpreted by Stearn (2020) to agree with the previously discussed findings of Renjith (2014), resulting from partial dissolution as the parential melt mixes with a more primitive (Ca-rich) melt. Within crystals from both populations, large sections of zoning within the mantle of the phenocryst have been removed via a significant resorption surface, which is attributed to a major mixing event,

resulting in significant changes to both the composition and temperature of the melt interacting with the plagioclase phenocrysts. These resorption surfaces can be found to varying degrees in crystals across all populations and eruptions. Immediately adjacent to the core for most crystals in both populations is a section of reverse zoning, providing additional credence to the interpretation of a major mixing event within the magma chamber (Figure 3). It should be noted that reverse zoning is not isolated at resorption surfaces, preventing the interpretation of the reverse zoning as being a result of inherited cores. Progressing from the reverse zoning towards the rim of the phenocryst, the plagioclase show less dramatic growth textures, with either low amplitude oscillatory zoning or normal zoning present until the rim of the phenocryst (Figure 3).

Within Stage II (Type IIa plagioclase), plagioclase phenocrysts exhibit no sieving within the core or rim, but contain widespread pockets of resorption, and have oscillatory zoning in the mantle which progresses until normal zoning initiates at the rim. This records fluctuating conditions within the magma chamber that presents itself as resorbed zones and oscillatory zoning. This instability ceases prior to eruption as the presence of normal zoning indicates fractional crystallization within the magma body. Within plagioclase transects, Mg, Fe, Sr, and Ba contents are either relatively consistent across the crystal from core to rim (variation of ~300 ppm), or exhibit consistent Fe and Sr contents, with elevated Mg and Ba contents in the core when compared to the rest of the transect.

In Stage III (Types IIb, III, IV, & V), phenocrysts with both coarse and fine sieving are present alongside varying degrees of resorption. This indicates dissolution via adiabatic decompression and interaction with magma of a more primitive composition (Renjith, 2014). This interpretation is supported by the presence of reverse zoning seen in phenocrysts from every eruption. Both normal and oscillatory zoning are present suggesting fluctuating conditions within

the magma chamber. Plagioclase transects from Stage III commonly exhibit steady Sr contents from core to rim, with an elevated spike in Mg, Fe, and Ba contents within the mantle directly adjacent to the core or at the rim of the phenocryst. These elevated values then progressively decrease towards the furthest extent (rim) of the transect. This pattern is seen in crystals from both eruptions, with the only difference between crystals from the Tumbres eruption and the Talabre lava is the location of the spike in contents. For the Talabre lava, this spike is present in the mantle adjacent to the core, whereas in the Tumbres eruption the elevated values are found at the rim.

Stage IV (I, IIa, III, IV) does not exhibit the same textures as Stages II and III, as this stage contains the only occurrences of unzoned plagioclase. Unlike all of the other analyzed phenocrysts, the growth of these plagioclase have only been impacted by slowly evolving melt composition by fractional crystallization. These phenocrysts likely grew following the instability events recorded in other phenocrysts, but may also be sourced from a isolated smaller reservoir. Two patterns in trace element contents are seen within Stage IV plagioclase: consistent contents of Mg, Fe, Sr, and Ba across the transect, and a large section of elevated Mg, Fe, and Ba contents centered at the middle of the transect (with Sr constant contents). These trace element patterns are seen within both the light dacitic and the banded pumice endmembers of the April 1993 plinian eruption, suggesting a common origin for these phenocrysts, or at least a common history of events during storage.

Recorded within the phenocrysts is evidence of one large mixing event per stage of Láscar's history, followed by either fractional crystallization or several smaller influxes of fresh melt within the magma body prior to the eruption. Additional zonation is present between the section of reverse zoning and the rim of the phenocryst, these mixing events likely pushed the

magmatic system towards eruption, but did not trigger it directly. Further evidence of a major mixing event is present with the distinct banding seen within erupted units from the Soncor Ignimbrite, Tumbres eruption, and the April 1993 plinian eruption, whose formation can be attributed to incomplete mixing of melts of two different compositions (Clynne, 1999): those being the host magma (light dacitic pumice) and an injection of more mafic magma (darker mafic pumice; Blum-Oeste & Wörner, 2016; Wörner *et al.*, 2018). This is supported by the changing temperature and pressure conditions, as well as the compositional changes that occurred within the magma chamber, as supported by the textures seen and the differing compositions present at the cores, mantles, and rims of the analyzed phenocrysts (Figure 8). These changing conditions within the magma chamber are evidenced within Sr, Mg, Ba, and Fe concentrations, as well as concentrations of rare earth element (REE), that exhibit disordered variation across individual plagioclase phenocrysts in both spot and line transects across all eruptions of interest.

This phenomena was noted by Stearn (2020) who attributed the differences between core and rim growth to represent a magma plumbing system with multiple smaller chambers at both shallow levels and at depth. Mixing events, such as those recorded as reverse zoning within plagioclase phenecrysts, provides a potential trigger for Láscar's larger eruptive events. The normal zoning seen corresponds to quiescent behavior prior to eruption and fractional crystallization of the magma chamber leading to the buildup of free-phase volatiles eventually leading to eruption, whereas low amplitude oscillatory zoning can be attributed to the numerous "small pulse" phreatic events that punctuate the time between larger eruptions at the volcanic center. It is the action of these numerous minor phreatic events that may provide the pathways needed for the larger eruptive events to occur. However, magma mixing cannot be attributed as

the only cause of eruption due to the presence of oscillatory and normal zoning between the resorption surfaces and the rim. This indicates conditions within the magma chamber returning to small-scale fluctuations and fractional crystallization prior to the eruption containing the plagioclase phenocrysts of interest.

Sr-Mg Diffusion Chronometry

The budding field of petrochronology is of recent interest to the disciplines of volcanology and petrology. One component of which seeks to discern the duration and rates of processes within the magmatic system such as cooling rates for volcanic bodies, crystal growth rates, and magma residence times utilizing major igneous minerals (e.g., olivine, plagioclase, and pyroxene) whose presence is ubiquitous within volcanic eruptive products (Engi *et al.*, 2017). Of particular interest to this project is the usage of diffusion to delimit the duration of the aforementioned thermal events through the modeling of the time-dependent flux of elemental components in response to compositional gradients (Engi *et al.*, 2017). Unlike other methods of obtaining magmatic timescales such as observational and radiometric, diffusive methods are not restricted to the timescales of isotopic decay schemes or to observations and measurements that occur in real-time (Dohmen *et al.*, 2017).

Diffusion petrochronology is founded around the process that as a mineral grows within a magma chamber, it incorporates major and trace elements in accordance with changes in the surrounding melt (Dohmen *et al.*, 2017). Perturbations to the chemistry of the melt or physical parameters controlling uptake such as chemical changes, or pressure, temperature, and redox conditions results in chemical changes between zones within the mineral (Dohmen *et al.*, 2017). These parameters are recorded within the mineral as with the growth of a new zone, the previous

zone becomes isolated from the melt, resulting in chemical potential gradients between successive zones (Dohmen *et al.*, 2017). As diffusion is a thermally mediated process by which it occurs at an expedited rate at higher temperatures and effectively quenches once a closure temperature is reached, diffusion chronometry is an effective tool to constrain the timescale between chemical perturbation and closure upon eruption, allowing for the determination of plagioclase residence times at near-liquidus conditions (Dohmen *et al.*, 2017; Fabbro *et al*., 2017).

The process of diffusion can be described as the random relative motion of one or more particles of a system relative to other particles of the same system, occurring in all materials at all times above the absolute zero (Costa *et al.*, 2008). This random motion becomes a directed flux in the presence of a chemical potential gradient, influencing the flow of matter towards the direction of decreasing chemical potential (Zhang, 2010). It is the action of directed fluxes that act to homogenize concentration gradients that is of particular interest, as it allows for the determination of plagioclase residence ages at warm and eruptible temperatures, as diffusion occurs at all temperatures, but only at an expedited rate when of a high enough temperature to allow for flexibility in the crystal lattice as diffusivity increases rapidly with temperature following the Arrhenius relationship (Zhang, 2010; Dohmen *et al.*, 2017).

A complication to modeling that immediately arises is the prevalence of disequilibrium textures within the majority of plagioclase phenocrysts. In this case, dissolution of the phenocryst acts to remove or erase parts of the "time" recorded within the phenocryst (Costa *et al.*, 2008). Additionally, dissolution may occur simultaneously with growth of additional or existing zones, further complicating the timescales that are modeled. Therefore, it should be

understood that the effect of dissolution on modeling results will underestimate the resulting timescales (Costa *et al.*, 2008).

To obtain modeled plagioclase residence times, this study utilizes an open-source Python diffusion script of the forward modeling of Sr and Mg in plagioclase using the finite difference approach of Costa *et al.* (2008), utilizing methods for determining partition coefficients (Mg: -26.1 ± 1.1, -25.7 ± 0.7; Sr: -30.4 ± 1.1, 28.5 ± 0.) from Bindeman *et al.* (1998), and function for determining diffusion coefficients for Sr and Mg from Van Orman *et al.* (2014). The full methodology is detailed in Lubbers *et al.* (2020). Modeling utilizes a combination of Sr and Mg trace element transects acquired via laser ablation ICP-MS and EPMA major element spot transects. Multiple elements have been utilized to provide additional constraints to the resulting modeled residence times. Plagioclase phenocrysts from the Tumbres-Talabre sequence (P02 & 25T-01; 6 crystals over 8 transects) and the April 1993 plinian eruption (P03 & P03A; 16 crystals over 24 transects) were modeled with a focus on phenocrysts from the April 1993 eruption. Due to the differing nature of the two datasets, An contents from the spot analyses are divided evenly across the length of the laser ablation transects, as a single EPMA spot was taken per distinct rim composition observed. A summary table of modeled Sr and Mg residence time ages, alongside their 2σ error can be found in Table 3. Models for each plagioclase phenocryst analyzed can be found in Appendix IV.

As temperature has a significant influence on the rate of diffusion, and by extension, residence times sourced from diffusion modeling, timescales of residence can be lengthened or shortened by adjusting the initial conditions of partition coefficients and temperature. The partition coefficient for a given element is calculated based on anorthite content according to the Arrhenius relationship as originally defined by Blundy & Wood (1991). Methods for obtaining

diffusion coefficients for Mg are from Costa *et al.* (2003) and Van Orman *et al.* (2014), whereas, methods for determining the Sr diffusion coefficient is sourced from Druitt *et al.* (2012). The temperature used for the purposes of modeling is 750 °C (1023.15 K), with geothermometry estimates from Matthews *et al.* (1994) falling between a consistent range of 890-970 °C, noting that pyroxene and oxide thermometry do not always give consistent results in pumices, due to the possible mixing of different populations of pyroxenes before oxide growth (Matthews *et al.,* 1994). Storage temperatures of pyroxenes were determined by Stearn (2020) and ranged from 861-1115 °C. Neither of these temperatures were used for modeling as they are not applicable for plagioclase. If a higher temperature were to be utilized for modeling, resulting residence times would be expected to be shorter as a result.

The results of the diffusion modeling are illustrated in Figure 11 and presented in Table 3. The majority of modeled plagioclase residence times falling within the decadal to centennial scale, with modeled residence times plotting close to the 1:1 correlation line for Mg and Sr best-fit ages (Figure 11). The deviation from this line is attributed to lost time due to disequilibrium (resorption) or by obtaining equilibrium of Mg in the phenocryst. This occurs because of the differing rates of diffusion for Mg and Sr, where Mg can completely diffuse out within decades whereas Sr diffusion will continue to progress for several centuries within the crystal lattice (Costa *et al.*, 2020; Costa, 2021). This descrepancy in timescales being due to the vastly different sizes of Mg and Sr, which ultimately affects the rate of diffusion across the crystal lattice via vacancies or defect-driven processes resulting from point defects within the crystal lattice or substitution in a Ca site (Cherniak, 2010; Dohmen *et al.*, 2017). Average residence times for the modeled eruptions (Tumbres eruption, Talabre lava, and April 1993 plinian eruption) have slightly decreased over time with plagioclase phenocrysts from the Tumbres eruption showing

the least variability in modeled best-fit residence ages (Figure 11). The average residence ages for all eruptions is longer for models using Sr diffusion than Mg diffusion, which should be expected due to the previously mentioned difference in diffusion rates. For Stage III, the average residence times are 68 years and 333 years for Mg and Sr, respectively, with ranges of 10 to 145 years and 71 to 780 years. For Stage IV, the average residence times are 29 years and 232 years for Mg and Sr, respectively, with ranges of 0.1 to 253 years and 0.1 to 2,832 years.

These results are in accordance with those of Viccaro *et al.* (2016), which found similar plagioclase residence ages on the decadal to centennial scale, with the residence times of recent phenocrysts being shorter than those from historical eruption of Mt. Etna. Viccaro *et al.* (2016) attributes this decrease in residence times with a gradual increase in eruption volume and eruption frequency rates through time, as a result of the increasing influence of extensional tectonic structures within the upper crust. However, due to the significant differences in the regional geology of the two centers, we instead attribute the increasing eruptive frequency to shortening timescales between small-volume influxes of more mafic melt that ascend through the crust without intercepting or developing voluminous magma reservoirs and associated crystal mush bodies, as proposed by Wörner *et al.* (2018) for young, monogenetic centers in the Central Andes. This is the same model that has been proposed to be the driving force behind the shifting magmatic regimes between Parinacota's Old Cone and Young Cone (Ginibre & Wörner, 2007; Wörner *et al.*, 2018) The eruptions of interest in this study are the largest from their respective stages in Láscar's history, and the bypassing or development of magma reservoirs agrees with both the geophysical studies focused upon Láscar as well as the short residence timescales derived from Sr-Mg diffusion modeling. An influx of hot primitive magma would allow for the

rejuvination of rhealogically-locked mush bodies (Cooper & Kent, 2014) and allow for the process of diffusion prior to the initiation of eruption.

As described by Ginibre & Wörner (2007), from the Old Cone to the Young Cone, resorption events and the effects of mafic recharge recorded in plagioclase become more abundant and prominent, which indicated a significant change in Parinacota's magma system following cone collapse in response to increased recharge rate. This interpretation is further supported by similar plagioclase zoning and textures seen both at Láscar and within the Healing Flows samples of Parinacota's Young Cone (Ginibre & Wörner, 2007). This quick ascension of more mafic magma through the crust would agree with the findings of Robidoux *et al.* (2020) whose geochemical analyses found that the mafic origin of most Láscar eruptive products reflect low magma differentiation and correspond to a more homogeneous source, exhibiting a typical volcanic arc signature with a low crustal influence. This extent of MORB modification within magma from Láscar Volcano was intepreted to potentially represent shorter residence times for the underlying magmatic systems, and is in agreement with the results of modeled Mg-Sr diffusion residence times (Robidoux *et al.*, 2020).

Attributing the increasing eruptive frequency to the injection of small batches of more mafic melt would also be in agreement with the small eruptive volumes produced by Láscar's eruptions (Gardeweg *et al.*, 1998) and its juvenille nature when compared to the longer-lived volcanoes of the CVZ such as Aucanquilcha and Ollagüe (Feeley *et al.*, 1993; Grunder *et al.*, 2008). Furthermore, the relatively short residence times as modeled by Mg-Sr diffusion geospeedometry can be accommodated by a nearly full evacuation of eruptible magma within the magma chamber, as the plagioclase zonation observed has recorded only a major mixing event attributed to the previous eruption and small-pulse instability leading up to the eruption of origin.

The full evacuation hypothesis is supported by recent geophysical studies of Láscar, which have found no evidence for a long-lived mush body beneath the volcano (Díaz *et al*., 2012; Gaete *et al*., 2019), with previous studies suggesting the pressurization of a shallow magma chamber providing the source for Láscar's major eruptions (Matthews *et al*., 1997). Additionally, in many cases it has been found that crystal mush reservoirs at low melt fractions fall within the resolution of tomographic imaging by seismic and magnetotelluric methods, and therefore, may be undetectable by these sensing techniques (Pritchard *et al*., 2018; Weber *et al*., 2023). Therefore, the current behavior of Láscar's magmatic system can be interpreted as mixing events (causing sieving and resorption surfaces) which are attributed to the volcanic center's larger eruptions, with intermittent smaller-volume influxes of more mafic melt (resulting in low amplitude oscillatory zoning and normal zoning) that are expressed as the more frequent minor phreatic eruptions. The presence of resorbed cores within plagioclase crystal populations also may suggest the presence of rhealogically-locked sub-solidus crystal mushes (Cooper & Kent, 2014). These crystal mushes are present beneath Láscar in cold-storage conditions, and are reactivated by influxes of new more-primitive melt into the system.

CONCLUSION

Plagioclase crystal residence ages sourced from Sr and Mg diffusion should be considered as "near-liquidus residence times" and likely significantly underestimate the true residence times of the plagioclase at Láscar (Fabbro *et al*., 2017). This is because diffusion is largely a temperature dependent process (Costa *et al*., 2020), and can be limited when magma chambers are maintained at a lower temperature and rhealogically-locked, preventing eruptions from occurring (Cooper & Kent, 2014). This means that the true ages of the plagioclase cannot be determined through these methods, but rather the residence ages can provide insight into how long the modeled phenocrysts were kept in a warm, eruptible state before their dated eruption (Fabbro *et al*., 2017). The timescale of storage at near-liquidus temperatures is of additional importance as recent research has shown that timescales as determined via diffusion geochronometry are on the same order of magnitude as the recorded eruptive frequency of the volcanoes from which they are sourced (Costa *et al*., 2020). Therefore, when combined with an array of volcanic sensing and monitoring techniques such as monitoring borehole strain, seismic activity, and gas emission chemistry, modeled near-liquid residence times will provide additional insight into the timescales from volcanic unrest to activity and contribute to a better assessment of volcanic hazards at Láscar (Costa *et al*., 2020).

We applied paired Sr-Mg diffusion modeling in plagioclase from the Tumbres eruption, Talabre lava, and both the banded and non-banded endmembers of the April 1993 plinian eruption of Láscar Volcano to gain insight into the long-term magma storage conditions of a volcanic center outside the proposed boundaries of the Altiplano-Puna Magma Body. Our results indicate concurrence between plagioclase trace element geochemistry and petrologic textural

analysis, indicating open-system magma mixing processes. Plagioclase from Láscar are recording timescales of decades to centuries at near-liquidus conditions, which we interpret to coincide with the eruptive style of small-pulse phreatic eruptions punctuated by larger explosive eruptive events, which are caused by the influx of small-volumes of more mafic melt that ascend without intercepting or developing large magma or mush bodies, similarly to what has been proposed for the activity regime of Parinacota's Young Cone (Ginibre & Wörner, 2007; Wörner *et al.*, 2018).

Plagioclase petrographic textures that indicate mixing with more primitive composition melts (reverse zoning), as well as instability within the magma chamber (oscillatory zoning, coarse/fine sieving, resorption) that is followed by quiescence and compositional evolution by fractional crystallization (normal zoning) in all stages at Láscar. Additional oscillatory zoning is present between the reverse zoning in the mantle and normal zoning at the rim, this mixing event likely primes the system towards eruption, but not the initiation of the event. Plagioclase chemistry supports the previously described "small batch model" as major and trace element compositions between cores and rims do not fall within defined populations across all eruptions. The relative short residence times as recorded within Láscar agree with the results of Robidoux *et al.* (2020) who hypothesized shorter residence times within Láscar's magmatic system based upon the extent of MORB modification within magma from Láscar. These results help to constrain the long-term magma storage conditions of juvenile intermediate-composition magma systems outside the influence of the Altiplano-Puna Magma Body in the Central Andes and can be applied alongside further volcano monitoring techniques to provide additional insight into Láscar's eruptive behavior.

REFERENCES

Aguilera Brazza, F. (2018). Lascar Volcano Field Guide, Sept. 1-8, 2018, San Pedro de Atacama, N. Chile. *State of the Arc Meeting* 7.

Allmendinger, R.W., Jordan, T.E., Kay, S.M., & Isacks, B.L. (1997). The Evolution of the Altiplano-Puna Plateau of the Central Andes. *Annual Review of Earth and Planetary Science* 25, 139-174.

Berlo, K., Blundy, J., Turner, S., & Hawkesworth, C. (2007). Textural and chemical variation in plagioclase phenocrysts from the 1980 eruptions of Mount St. Helens, USA. *Contributions to Mineralogy and Petrology* 154, 291-308.

Bindeman, I.N., Davis, A.M., & Drake, M.J. (1998). Ion microprobe study of plagioclase-basalt partition experiments at natural concentration levels of trace elements. *Geochimica et Cosmochimca Acta* 62, 1175-1193.

Blum-Oeste, M., & Wörner, G. (2016). Central Andean magmatism can be constrained by three ubiquitous endmembers. *Terra Nova* 28, 434-440.

Blundy, J.D., & Wood, B.J. (1991). Crystal-Chemical Controls on the Partitioning of Sr and Ba between Plagioclase Feldspar, Silicate Melts, and Hydrothermal Solutions. *Geochimica et Cosmochimica Acta* 55, 193-201.

Calder, E.S., Sparks, R.S.J., & Gardeweg, M.C. (2000). Erosion, transport and segregation of pumice and lithic clasts in pyroclastic flows inferred from ignimbrite at Lascar Volcano, Chile. *Journal of Volcanology and Geothermal Research* 104, 201-235.

Cherniak, D.J. (2010). Cation Diffusion in Feldspars. *Reviews in Mineralogy and Geochemistry* 72, 691-733.

Clynne, M. (1999). A Complex Magma Mixing Origin for Rocks Erupted in 1915, Lassen Peak, California. *Journal of Petrology* 40, 105-132.

Cooper, K.M., & Kent, A.J.R. (2014). Rapid remobilization of magmatic crystals kept in cold storage. *Nature Letters* 506, 480-483.

Costa, F., Chakraborty, S., & Dohmen, R. (2003). Diffusion coupling between major and trace elements and a model for the calculation of magma chamber residence times using plagioclase. *Geochimica et Cosmochimica Acta* 67, 2189-2200.

Costa, F., Dohmen, R., & Chakraborty, S. (2008). Time Scales of Magmatic Processes from Modeling the Zoning Patterns of Crystals. *Reviews in Mineralogy & Geochemistry* 69, 545-594.

Costa, F., Shea, T., & Ubide, T. (2020). Diffusion chronometry and the timescales of magmatic processes. *Nature* 506, 480-483.

Costa, F. (2021). Clocks in Magmatic Rocks. *Annual Reviews of Earth and Planetary Sciences* 49, 231-252.

Davidson, J., Turner, S., & Plank, T. (2013). Dy/Dy*: Variations Arising from Mantle Sources and Petrogenetic Processes. *Journal of Petrology* 54, 525-537.

Déruelle, B., Figueroa, O., Medina, E., Viramonte, J., & Maragaño, M. (1996). Petrology of pumices of April 1993 eruption of Lascar (Atacama, Chile). *Terra Nova* 8, 191-199.

de Silva, S.L. (1989). Altiplano-Puna volcanic complex of the central Andes. *Geology* 17, 1102-1106.

de Zeeuw-van Dalfsen, E., Richter, N., González, G., & Walter, T.R. (2017). Geomorphology and structural development of the nested summit crater of Láscar Volcano studied with Terrestrial Laser Scanner data and analogue modelling. *Journal of Volcanology and Geothermal Research* 329, 1-12.

Díaz, D., Brasse, H., & Ticona, F. (2012). Conductivity distribution beneath Lascar volcano (northern Chile) and the Puna, inferred from magnetotelluric data. *Journal of Volcanology and Geothermal Research* 217-218, 21-29.

Dohmen, R., Faak, K., & Blundy, J.D. (2017). Chronometry and Speedometry of Magmatic Processes using Chemical Diffusion in Olivine, Plagioclase, and Pyroxenes. *Reviews in Mineralogy and Geochemistry* 88, 535-575.

Druitt, T.H., Costa, F., Deloule, E., Dungan, M., & Scaillet, B. (2012). Decadal to monthly timescales of magma transfer and reservoir growth at a caldera volcano. *Nature Letters* 482, 77- 80.

Engi, M., Lanari, P., & Kohn, M.J. (2017). Significant Ages—An Introduction to Petrochronology. *Reviews in Mineralogy & Geochemistry* 83, 1-12.

Fabbro, G.N., Druitt, T.H., & Costa, F. (2017). Storage and Eruption of Silicic magma across the Transition from Dominantly Effusive to Caldera-forming States at an Arc Volcano (Santorini, Greece). *Journal of Petrology* 58, 2429-2464.

Feeley, T.C., Davidson, J.P., & Armendia, A. (1993). The volcanic and magmatic evolution of Volcán Ollagüe, a high-K, late Quaternary stratovolcano in the Andean Central Volcanic Zone. *Journal of Volcanology and Geothermal Research* 54, 221-245.

Francis, P.W., & Rothery, D.A. (1987). Using the Landsat Thematic Mapper to detect and monitor active volcanoes: An example from Lascar volcano, northern Chile. *Geology* 15, 614-617.

Francis, P.W., Glaze, L.S., & Rothery, D.A. (1989). Lascar Volcano set to erupt? *Nature* 339, 434.

Gaete, A., Cesca, S., Franco, L., San Martin, J., Cartes, C., & Walter, T.R. (2019). Seismic activity during the 2013-2015 intereruptive phase at Lascar volcano, Chile. *Geophysical Journal International* 219, 449-463.

Gaete, A., Walter, T.R., Bredemeyer, S., Zimmer, M., Kujawa, C., Marin, L.F., San Martin, J., & Bucarey Parra, C. (2020). Processes culminating in the 2015 phreatic explosion at Lascar volcano, Chile, evidenced by multiparametric data. *Natural Hazards and Earth System Sciences* 20, 377-397.

Gardeweg, M.C., Sparks, S.J., & Matthews, S.J. (1998). Evolution of Lascar Volcano, Northern Chile. *Journal of the Geological Society, London* 155, 89-104.

Ginibre, C., Kronz, A., & Wörner, G. (2002). High-resolution quantitative imaging of plagioclase composition using accumulated backscattered electron images: new constraints on oscillatory zoning. *Contributions to Mineralogy and Petrology* 142, 436-448.

Ginibre, C., & Wörner, G. (2007). Variable parent magmas and recharge regimes of the Parinacota magma system (N. Chile) revealed by Fe, Mg, and Sr zoning in plagioclase. *Lithos* 98, 114-140.

Ginibre, C., Wörner, G., & Kronz, A. (2007). Crystal Zoning as an Archive for Magma Evolution. *Elements* 3, 261-266.

Global Volcanism Program. (1993). Report on Lascar (Chile) (Venzke, E., ed.). *Bulletin of the Global Volcanism Network* 18:4. Smithsonian Institution. https://volcano.si.edu/showreport.cfm?doi=10.5479/si.GVP.BGVN199304-355100

Global Volcanism Program. (2017). Report on Lascar (Chile) (Crafford, A.E. & Venzke, E., eds.). *Bulletin of the Global Volcanism Network* 42:7. Smithsonian Institution. https://volcano.si.edu/showreport.cfm?doi=10.5479/si.GVP.BGVN201707-355100

Global Volcanism Program. (2022). Report on Lascar (Chile) (Sennert, S.K., ed.). *Weekly Volcanic Activity Report, 14 December-20 December 2022*. Smithsonian Institution and US Geological Survey. https://volcano.si.edu/showreport.cfm?wvar=GVP.WVAR20221214-355100

Global Volcanism Program. (2023). Report on Lascar (Chile) (Sennert, S.K., ed). *Weekly Volcanic Activity Report, 8 February-14 February 2023.* Smithsonian Institution and US Geological Survey. https://volcano.si.edu/showreport.cfm?wvar=GVP.WVAR20230208-355100

González, C., Inostroza, M., Aguilera, F., González, G., Viramonte, J., & Menzies, A. (2015). Heat and mass flux measurements using Landsat images from the 2000-2004 period, Lascar volcano, northern Chile. *Journal of Volcanology and Geothermal Research* 301, 277-292.

Grunder, A., Klemetti, E.W., Feeley, T.C., & McKee, C.M. (2008). Eleven million years of arc volcanism at the Aucanquilcha Volcanic Cluster, northern Chilean Andes: implications for the life span and emplacement of plutons. *Transactions of the Royal Society of Edinburgh: Earth Sciences* 97, 415-436.

Harmon, R.S., Barreiro, B.A., Moorbath, S., Hoefs, J., Francis, P.W., Thorpe, R.S., Déruelle, B., McHugh, J., & Viglino, J.A. (1984). Regional O-, Sr-, and Pb-isotope relationships in late Cenozoic calc-alkaline lavas of the Andean Cordillera. *Journal of the Geological Society, London* 141, 803-822.

Hellweg, M. (2003). The polarization of volcanic seismic signals: medium or source? *Journal of Volcanology and Geothermal Research* 128, 159-176.

Jay, J., Welch, M., Pritchard, M.E., Mares, P.J., Mnich, M.E., Melkonian, A.K., Aguilera, F., Naranjo, J.A., Sunagua, M., & Clavero, J. (2013). Volcanic hotspots of the central and southern Andes as seen from space by ASTER and MODVOLC between the years 2000 and 2010. *The Geological Society, London, Special Publications* 380.

Jessop, D.E., Kelfoun K., Labazuy, P., Mangeney, A., Roche, O., Tillier, J.-L., Trouillet, M., & Thibault, G. (2012). LiDAR derived morphology of the 1993 Lascar pyroclastic flow deposits, and implication for flow dybamics and rheology. *Journal of Volcanology and Geothermal Research* 245-246, 81-97.

Jochum, K.P., Weis, U., Stoll, B., Kuzmin, D., Yang, Q., Raczek, I., Jacob, D.E., Stracke, A., Birbaum, K., Frick D.A., Günther, D., & Enzweiler, J. (2011). Determination of Reference Values for NIST SRM 610-617 Glasses Following ISO Guidelines. *Geostandards and Geoanalytical Research* 35, 397-429.

Johnson, D.M., Hooper, P.R., & Conrey, R.M. (1999). XRF analysis of rocks and minerals for major and trace elements on a single low dilution li-tetraborate fused bead. *Advances in X-Ray Analysis* 41, 843-867.

Kendrick, E., Bevis, M., Smalley Jr., R., Brooks, B., Barriga Vargas, R., Lauría, E., & Souto Fortes, L.P. (2003). The Nazca-South America Euler vector and its rate of change. *Journal of South American Earth Sciences* 16, 125-131.

Liu, Y., Hu, Z., Gao, S., Gunther, D., Xu, J., Gao, C., & Chen, H. (2008). In situ analysis of major and trace elements of anhydorus minerals by LA-ICP-MS without applying an internal standard. *Chemical Geology* 257, 34-43.

Lubbers, J., Kent, A.J.R., & de Silva, S. (2022). Thermal Budgets of Magma Storage Constrained by Diffusion Chronometry: the Cerro Galán Ignimbrite. *Journal of Petrology* 63, 1-19.

Manami, M., Tassara, A., & Wörner, G. (2008). Composition and structural control of crustal domains in the central Andes. *Geochemistry, Geophysics, Geosystems* 9, 1-13.

Manami, M., Wörner, G., & Sempere, T. (2010). Geochemical variations in igneous rocks of the Central Andean orocline (13°S to 18°S): Tracing crustal thickening and magma generation through time and space. *GSA Bulletin* 122, 162-182.

Matthews, S.J., Jones, A.P., & Gardeweg, M.C. (1994). Lascar Volcano, Northern Chile; Evidence for Steady-State Disequilibrium. *Journal of Petrology* 35, 401-432.

Matthews, S.J., Marquillas, R.A., Kemp, A.J., Grange, F.K., & Gardeweg, M.C. (1996). Active skarn formation beneath Lascar Volcano, northern Chile: a petrographic and geochemical study of xenoliths in eruption products. *Journal of Metamophic Geology* 14, 509-530.

Matthews, S.J., Gardeweg, M.C., & Sparks, R.S.J. (1997). The 1984 to 1996 cyclic activity of Lascar Volcano, northern Chile: cycles of dome growth, dome subsidence, degassing, and explosive eruptions. *The Bulletin of Volcanology* 59, 72-82.

Matthews, S.J., Sparks, S.J., & Gardeweg, M.C. (1999). The Piedras Grandes-Soncor Eruptions, Lascar Volcano, Chile; Evolution of a Zoned Magma Chamber in the Central Andean Upper Crust. *Journal of Petrology* 40, 1891-1919.

Mattioli, M., Renzulli, A., Menna, M., Holm, P.M. (2006). Rapid ascent and contamination of magmas through the thick crust of the CVZ (Andes, Ollagüe region): Evidence from a nearly aphyric high-K andesite with skeletal olivines. *Journal of Volcanology and Geothermal Research* 158, 87-105.

McDonough, W.F. & Sun, S. (1995). The composition of the Earth. *Chemical Geology* 120, 223-253.

Michelfelder, G.S., Feeley, T.C., Wilder, A.D., & Klemetti, E.W. (2013). Modification of the Continental Crust by Subduction Zone Magmatism and *Vice-Versa*: Across-Strike Geochemical Variations of Silicic Lavas from Individual Eruptive Centers in the Andean Central Volcanic Zone. *Geosciences* 3, 633-677.

Montgomery, D.R., Balco, G., & Willet, S.D. (2001). Climate, tectonics, and the morphology of the Andes. *Geology* 29, 579-582.

Oppenheimer, C., Francis, P.W., Rothery, D.A., Carlton, R.W.T., & Glaze, L.S. (1993). Infrared Image Analysis of Volcanic Thermal Features: Láscar Volcano, Chile, 1984-1992. *Journal of Geophysical Research* 98, 4269-4286.

Paton, C., Hellstrom, J., Paul, B., Woodhead, J., & Hergt, J. (2011). Iolite: Freeware for the visualization and processing of mass spectrometric data. *Journal of Analytical Atomic Spectrometry* 26, 2508-2518.

Pavez, A., Remy, D., Bonvalot, S., Diament, M., Gabalda, G., Froger, J.-L., Julien, P., Legrand, D., & Moisset, D. (2006). Insight into ground deformations at Lascar volcano (Chile) from SAR interferometry, photogrammetry and GPS data: Implications on volcano dynamics and future space monitoring. *Remote Sensing of Environment* 100, 307-320.

Pritchard, M.E., Henderson, S.T., Jay, J.A., Soler, V., Kzresni, D.A., Button, N.E., Welch, M.D., Semple, A.G., Glass, B., Sunagua, M., Minaya, E., Amigo, A., & Clavero, J. (2014). Reconnaissance earthquake studies at nine volcanic areas of the central Andes with coincident satellite thermal and InSAR observations. *Journal of Volcanology and Geothermal Research* 280, 90-103.

Pritchard M.E., de Silva, S.L., Michelfelder, G., Zandt, G., McNutt, S.R., Gottsman, J., West, M.E., Blundy, J., Christensen, D.H., Finnegan, N.J., Minaya E., Sparks, R.S.J., Sunagua, M., Unsworth, M.J., Alvizuri, C., Comeau, M.J., del Potro, R., Díaz, D., Diez, M., Farrell, A., Henderson, S.T., Jay, J.A., Lopez, T., Legrand, D., Naranjo, J.A., McFarlin, H., Muir, D., Perkins, J.P., Spica, Z., Wilder, A., & Ward, K.M. (2018). Synthesis: PLUTONS: Investigating the relationship between pluton growth and volcanism in the Central Andes. *Geosphere* 14, 954-982.

Renjith, M.L. (2014). Micro-textures in plagioclase from 1994-1995 eruption, Barren Island Volcano: Evidence of dynamic magma plumbing system in the Andaman subduction zone. *Geoscience Frontiers* 5, 113-126.

Robidoux, P., Rizzo, AL., Aguilera, F., Aiuppa, A., Artale, M., Liuzzo, M., Nazzari, M., & Zummo, F. (2020). Petrological and noble gas features of Lascar and Lastarria volcanoes (Chile): Inferences on plumbing systems and mantle characteristics. *Lithos* 370-371, 1-21.

Sainlot, N., Vlastélic, I., Nauret, F., Moune, S., & Aguilera, F. (2020). Sr-Pb isotopes signature of Lascar volcano (Chile): Insight into contamination of arc magmas ascending through a thick continental crust. *Journal of South American Earth Sciences* 101, 1-16.

Shcherbakov, V.D., Plechov, P.Y., Izbekov, P.E., & Shipman, J.S. (2010). Plagioclase zoning as an indicator of magma processes at Bezymianny Volcano, Kamchatka. *Contributions to Mineralogy and Petrology* 162, 83-99.

Sparks, R.S.J., Gardeweg, M.C., Calder, E.S., & Matthews S.J. (1997). Erosion by proclastic flows on Lascar Volcano, Chile. *Bulletin of Volcanology* 58, 557-565.

Stearn, M. (2020). Pumice Compositions and Mineral Chemistry from Lascar Volcano, Chile. *MSU Graduate Theses* 3517, 1-85.

Smithsonian Institution National Museum of Natural History (2013). Global Volcanism Program (Láscar). https://volcano.si.edu/volcano.cfm?vn=355100 (accessed 14 March 2023).

Tassi, F., Aguilera, F., Vaselli, O., Medina, E., Tedesco, D., Delgado Huertas, A., Poreda, R., & Kojima, S. (2008). The magmatic- and hydrothermal-dominated fumarolic system at the Active Crater of Lascar volcano, northern Chile. *Bulletin of Volcanology* 71, 171-183.

Tepley III, F.J., Davidson, J.P., Tilling, R.I., & Arth, J.G. (2000). Magma Mixing, Recharge and Eruption Histories Recorded in Plagioclase Phenocrysts from El Chicón Volcano, Mexico. *Journal of Petrology* 41, 1397-1411.

Van Orman, J.A., Cherniak, D.J., & Kita, N.T. (2014). Magnesium diffusion in plagioclase: dependence on composition, and implications for thermal resetting of the 26Al-26Mg early solar system chronometer. *Earth and Planetary Science Letters* 385, 79-88.

Viccaro, M., Barca, D., Bohrson, W.A., D'Oriano, C., Giuffrida, M., Nicotra, E., & Pitcher, B.W. (2016). Crystal residence times from trace element zoning in plagioclase reveal changes in magma transfer dynamics at Mt. Etna during the last 400 years. *Lithos* 248-251, 309-323.

Ward, K.M., Zandt, G., Beck, S.L., Christensen, D.H., & McFarlin, H. (2014). Seismic imaging of the magmatic underpinnings beneath the Altiplano-Puna volcanic conplex from the joint inversion of surface wave dispersion and receiver functions. *Earth and Plantery Science Letters* 404, 43-53.

Weber, G., Blundy, J., & Bevan, D. (2023). Mush Amalgamation, Short Residence, and Sparce Detectability of Eruptible Magma Before Andean Super-Eruptions. *Geochemistry, Geophysics, Geosystems* 24, 1-24.

Woodhead J., Hellstrom, J., Hergt, J., Greig, A., & Maas, R. (2007). Isotopic and elemental imaging of geological materials by laser ablation Inductively Coupled Plasma mass spectrometry. *Journal of Geostandards and Geoanalytical Research* 31, 331-343.

Wooster, M.J. (2001). Long-term infrared surveillance of Lascar Volcano: contrasting activity cycles and cooling pyroclastics. *Geophysical Research Letters* 28, 847-850.

Wörner, G., Manami, M., & Blum-Oeste, M. (2018). Magmatism in the Central Andes. *Elements* 14, 237-244.

Zandt, G., Leidig, M., Chmielowski, J., Baumont, D., & Yuan, X. (2003). Seismic Detection and Characterization of the Altiplano-Puna Magma Body, Central Andes. *Pure and Applied Geophysics* 160, 789-807.

Zhang, Y. (2010). Diffusion in Minerals and Melts: Theoretical Background. *Reviews in Mineralogy & Geochemistry* 72, 5-59.

Table 1: Normalized Whole Rock Major Element Data (Weight %)

	Stage I				Stage II	Stage III	Stage IV		
	24-01	24-04	24-100	100	P01	P02	25T-01	P03	P03B
SiO_2	61.2	60.3	61	61.5	59.4	59	58.5	61	58.6
TiO_2	0.72	0.73	0.72	0.71	0.77	0.80	0.85	0.72	0.76
Al_2O_3	17.7	17.9	17.7	17.5	16.6	16.8	17.3	16.7	16.5
FeO*	5.27	5.32	5.29	5.09	5.77	6.26	6.42	5.70	6.49
MnO	0.10	0.10	0.10	0.10	0.10	0.12	0.11	0.11	0.12
MgO	2.33	2.39	2.36	2.26	3.72	3.81	3.43	3.43	4.80
CaO	5.74	5.79	5.73	5.74	6.09	6.73	7.09	6.02	7.08
Na_2O	3.97	3.86	3.97	3.94	3.37	3.39	3.78	3.37	2.23
K_2O	1.97	1.94	1.94	1.97	1.83	1.79	1.58	2.04	1.61
P_2O_5	0.24	0.23	0.23	0.23	0.21	0.25	0.31	0.19	0.18
Total	99.22	98.59	99.03	99.00	97.82	99.01	99.41	99.31	99.43
LOI %	0.78	1.41	0.97	1.00	2.18	0.99	0.59	0.69	0.57

Table 2: Unnormalized Whole Rock Trace Element Data (ppm)

	Stage I				Stage II	Stage III	Stage IV		
	24-01	24-04	24-100	100	P01	P02	25T-01	P03	P03B
La	22.14	26.52	27.02	25.0	24.27	23.00	23.20	23.42	20.87
Ce	42.59	54.35	52.09	51.3	53.44	54.59	46.51	52.56	49.73
Nd	21.63	26.30	26.47	24.6	23.88	22.86	24.03	22.67	20.13
Ba	414.0	452.12	505.54	451.	428.93	438.44	388.55	464.7	398.89
Th	15.53	7.56	15.59	7.49	13.37	10.00	13.15	10.46	12.94
Nb	11.19	9.50	13.86	9.40	12.87	11.54	14.92	12.08	7.40
Y	19.61	24.53	24.52	22.5	19.75	20.45	18.06	21.54	20.74
Hf	4.47	4.43	5.45	4.30	4.09	4.10	4.71	4.33	6.37
Ta	1.26	0.86	1.37	0.87	1.59	1.38	0.99	1.92	2.55
U	2.56	2.71	2.90	2.73	2.70	1.81	1.71	3.00	2.21
Pb	12.07	12.07	14.33	12.6	12.63	10.76	14.12	13.80	10.87
Rb	61.73	66.28	73.64	71.2	70.49	59.27	48.51	81.36	58.60
Cs	3.28	3.73	3.84	3.97	4.66	3.43	2.64	5.53	3.73
Sr	458.3	521.61	563.77	509.	555.07	585.92	705.48	467.8	500.51
Sc	12.25	12.88	19.28	12.5	19.63	23.43	20.47	22.72	26.44
Zr	154.0	167.29	192.82	166.	145.24	149.34	162.24	156.1	210.72
Sr/Y	23.37	21.26	22.99	22.5	28.11	28.65	39.05	21.72	24.13
Rb/Sr	0.13	0.13	0.13	0.14	0.13	0.10	0.07	0.17	0.12
Nb/Zr	0.07	0.06	0.07	0.06	0.09	0.08	0.09	0.08	0.04
Eu/Eu*	0.76	0.73	0.76	0.73	0.75	0.79	0.83	0.74	0.78
Dy/Dy	0.58	0.66	0.59	0.67	0.64	0.63	0.62	0.62	0.61
La/Yb_N	7.28	7.78	7.43	7.76	9.10	8.23	9.13	7.36	6.83

Table 3: Individual Results of Mg-Sr Diffusion Modeling

Sample	Grain	Mg Best Fit	Mg 2σ	Sr Best Fit	Sr 2σ
P02	P4-L1	49.4	31.94	71.1	52.21
P02	P4-L2	144.9	70.47	212.8	163.49
P02	P7-L1	10.1	7.16	270.6	45.48
P02	P7-L2	69.1	42.1	779.9	825.47
P03	P4-L2	*0.1*	*0.46*	1.1	0.89
P03	P5-L1	2.6	5.81	17.2	10.82
P03	P5-L2	4.9	4.43	40.3	36.7
P03	P7-L1	22.2	8.16	71.7	56.13
P03	P7-L2	5.5	3.33	36.4	21.35
P03	P8	9.8	9.64	174.4	52.17
P03	P11	55	31.21	99.3	72
P03	P12-L1	252.8	16.89	45.4	21
P03	P12-L2	5	1.95	29.3	8.27
P03	P13-L1	0.5	1.62	482	338.66
P03	P13-L2	7.9	5.68	0.1	2.01
P03A	P1-L1	26.8	16.22	274.7	161.25
P03A	P5-L1	26.8	16.22	274.7	161.25
P03A	P5-L2	9.3	3.49	161.9	75.56
P03A	P6	57	11.45	558.2	181.2
P03A	P7	17.4	10	0.1	1.02
P03A	P8-L1	7.6	3.56	58.2	44.06
P03A	P8-L2	18.6	13.6	126.4	93.7
P03A	P9	93.3	57.88	*76.8*	*77.43*
P03A	P12-L1	*0.1*	*0.17*	0.1	0.42
P03A	P12-L2	10	2.86	*0.2*	*0.23*
P03A	P13-L1	*0.1*	*0.21*	*0.1*	*0.17*
P03A	P13-L2	*0.1*	*0.21*	*0.1*	*0.17*
P03A	P18	21.3	2.49	*0.1*	*1.95*
25T1	P1	*51.5*	*94.73*	2832.5	2054.46
25T1	P3	34.2	21.16	*878.9*	*929.47*
25T1	P8	81.7	20.59	439.1	99.6
25T1	P9	0.1	0.09	0.1	0.07

Italicized portions of rows have 2σ error larger than the best fit age for the element of interest.

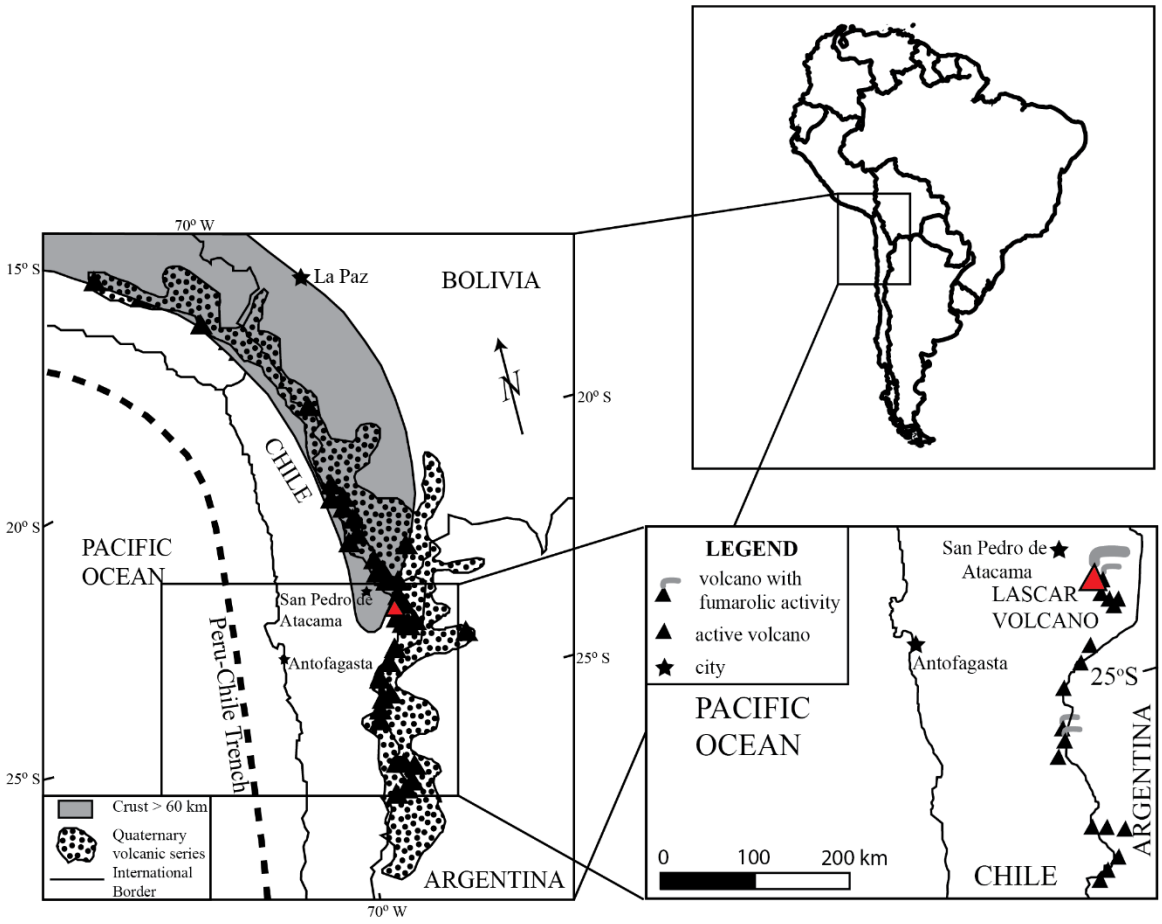

Figure 1: Location map of Láscar Volcano in reference to the trench-axis and other local volcanic and population centers.

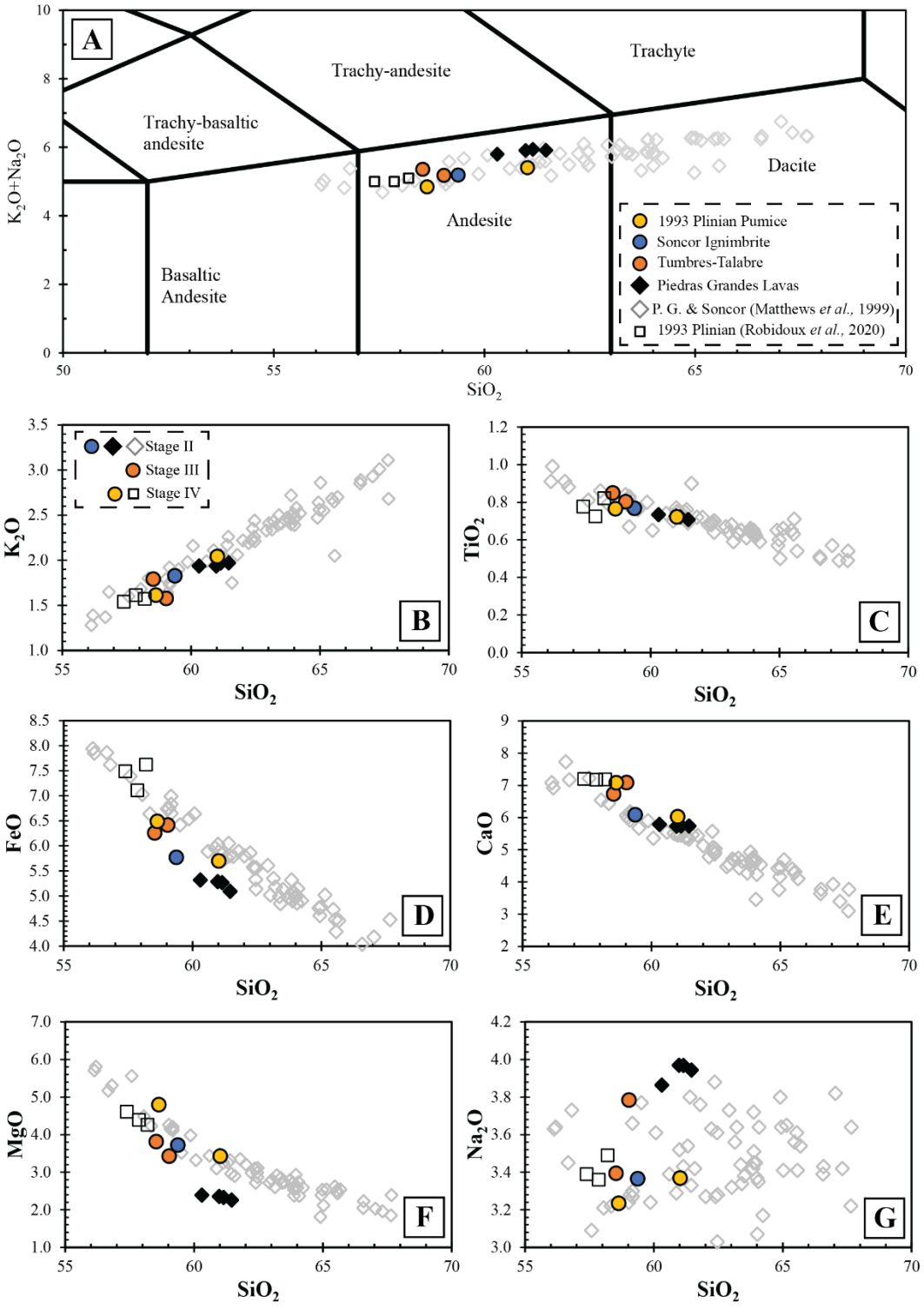

Figure 2: (A) Total alkalis versus silica (TAS) diagram of analyzed eruptions compared to data from Matthews *et al.* (1999) and Robidoux *et al.* (2020). (B - G) Whole rock major element variation diagrams from Láscar divided by stage.

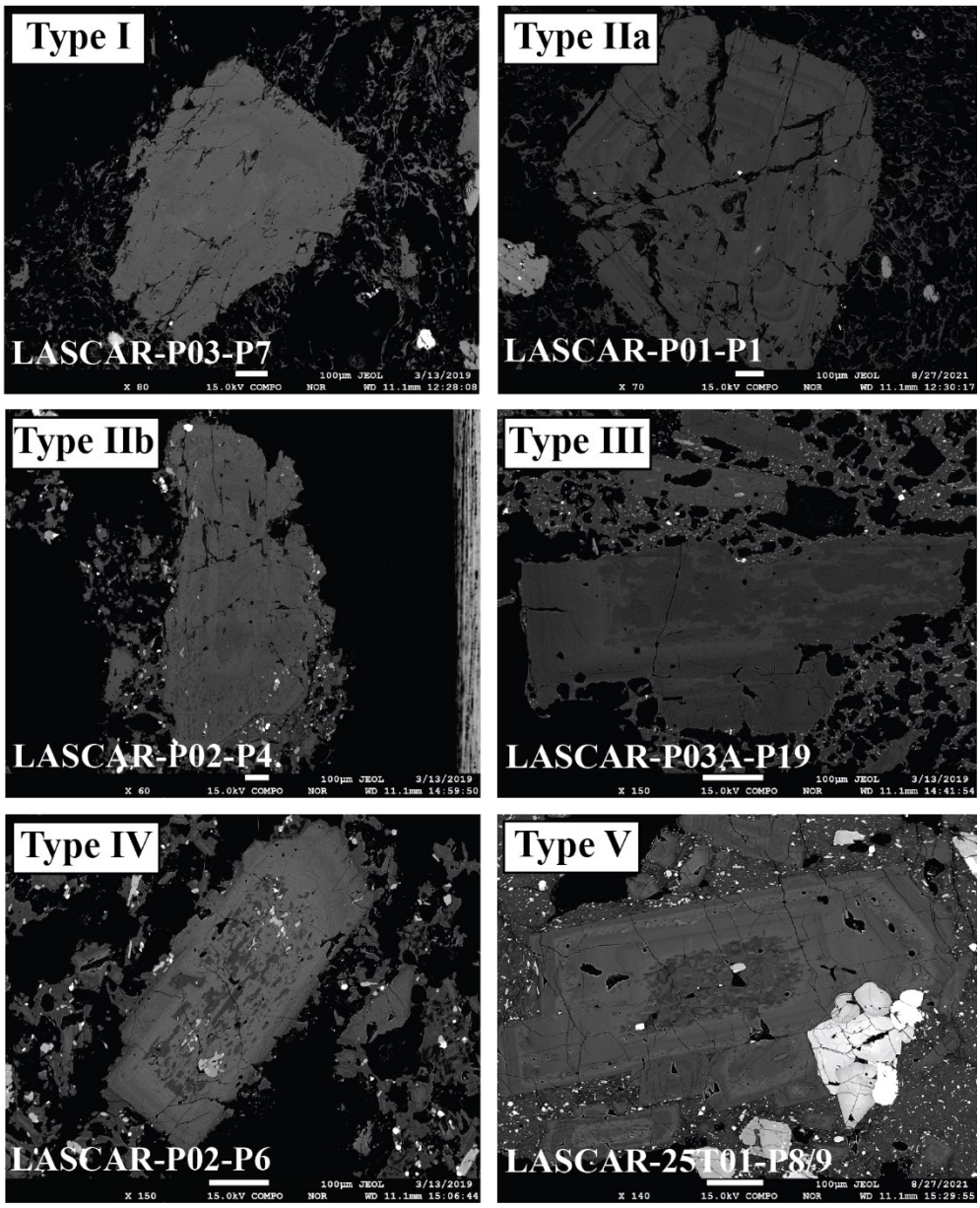

Figure 3: Backscattered electron images of representative plagioclase phenocrysts divided by textural population.

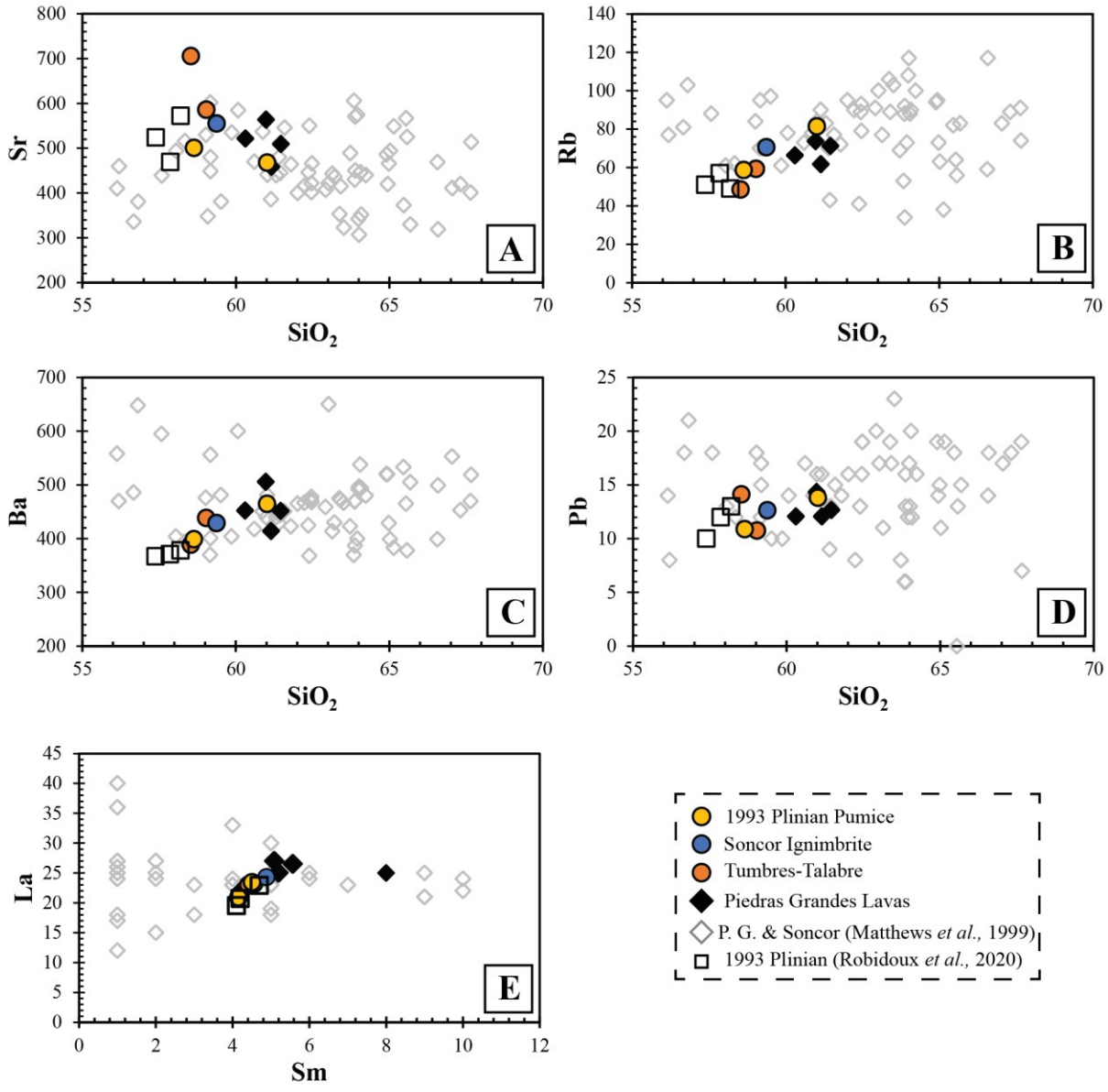

Figure 4: Whole rock trace element variation diagrams from Láscar divided by eruption.

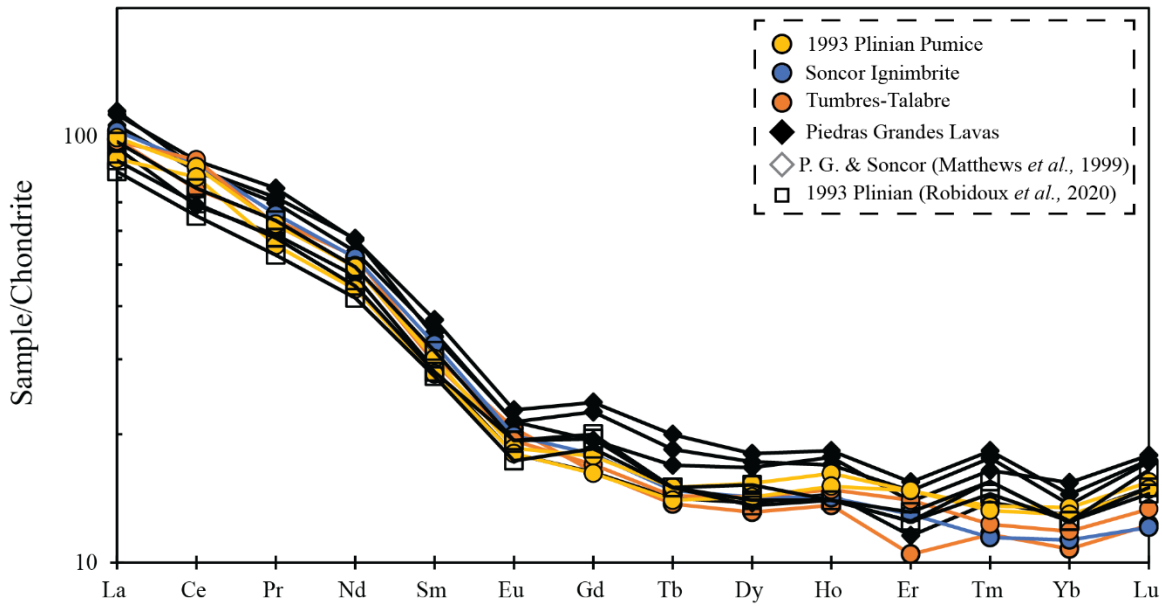

Figure 5: Rare earth element (REE) diagram of bulk whole rock analyses, normalized to chondrite (McDonough & Sun, 1995).

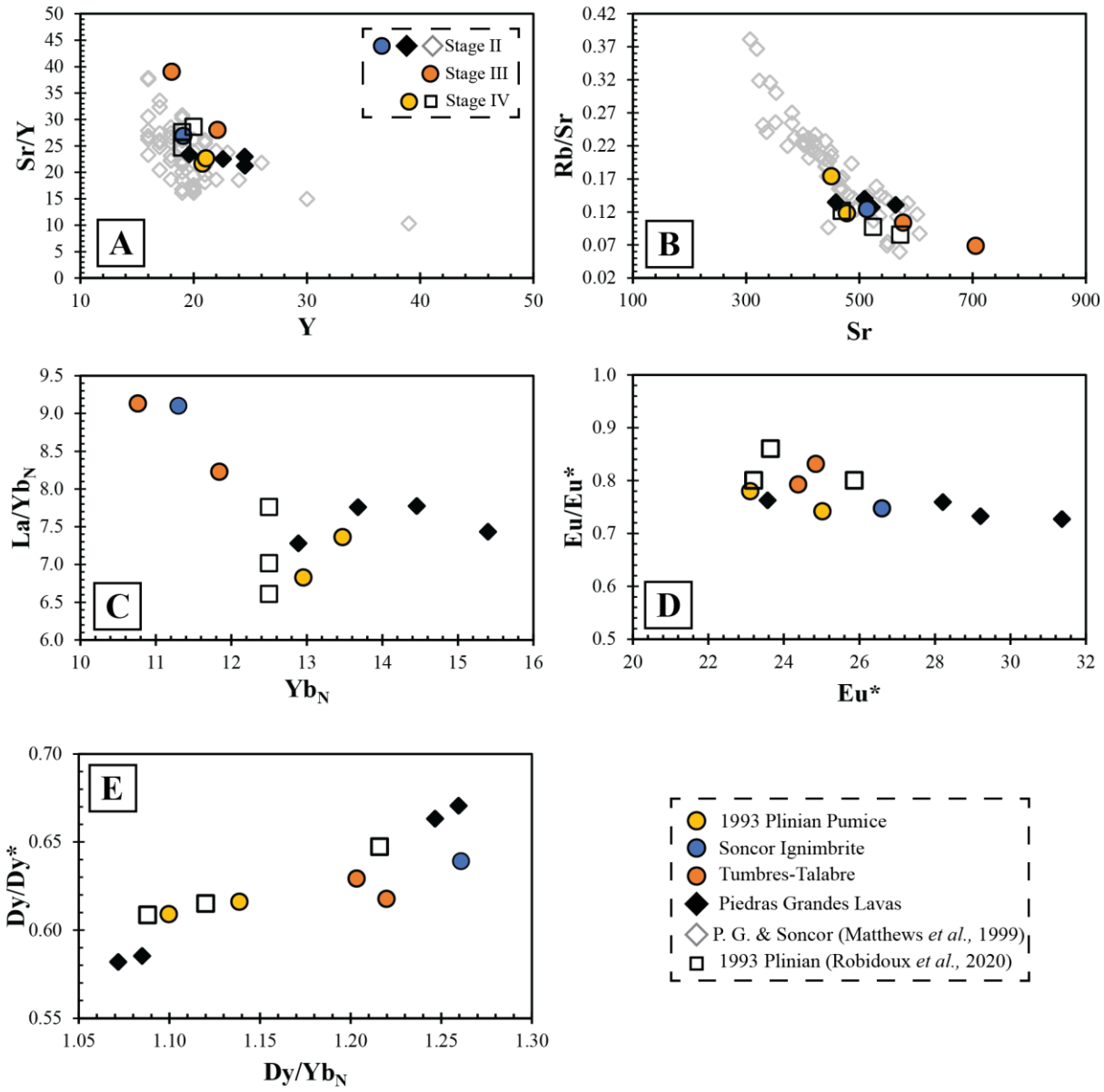

Figure 6: Trace element variation diagrams of selected trace element ratios for bulk whole rock analyses. Dy/Yb$_N$ has been normalized to chrondrite (McDonough & Sun, 1995). Dy/Dy* is calculated from Davidson *et al.* (2013).

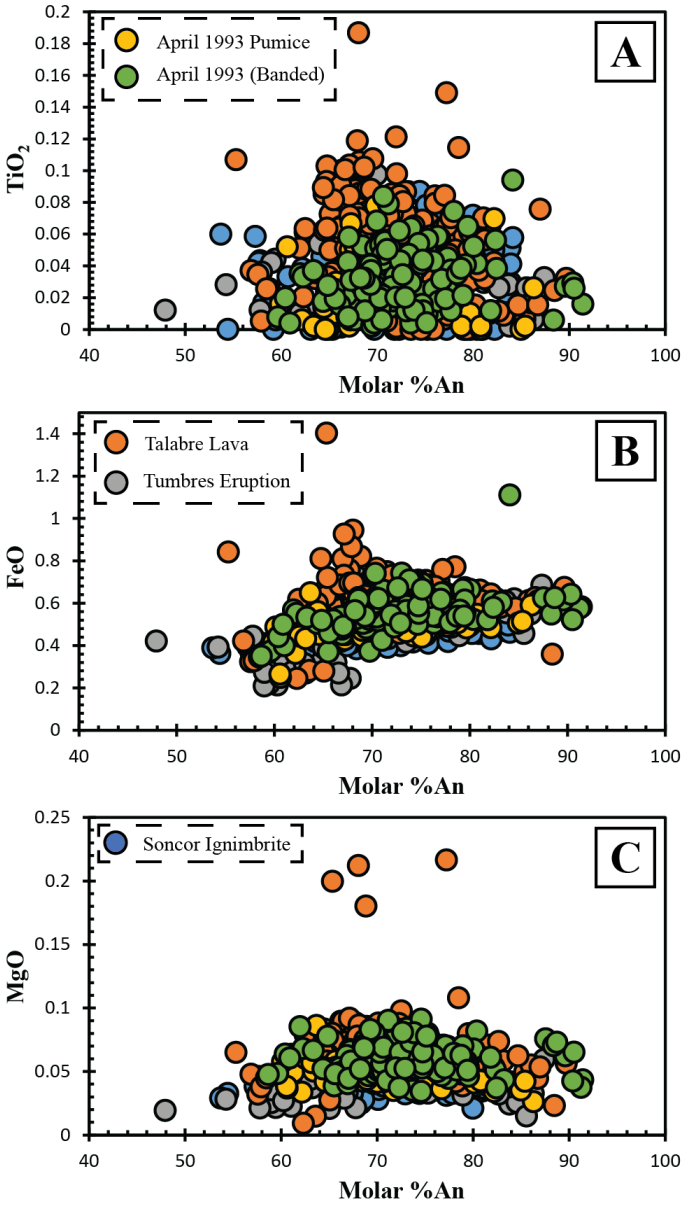

Figure 7: Major element variation diagrams of selected plagioclase major element compositions plotted against molar %An.

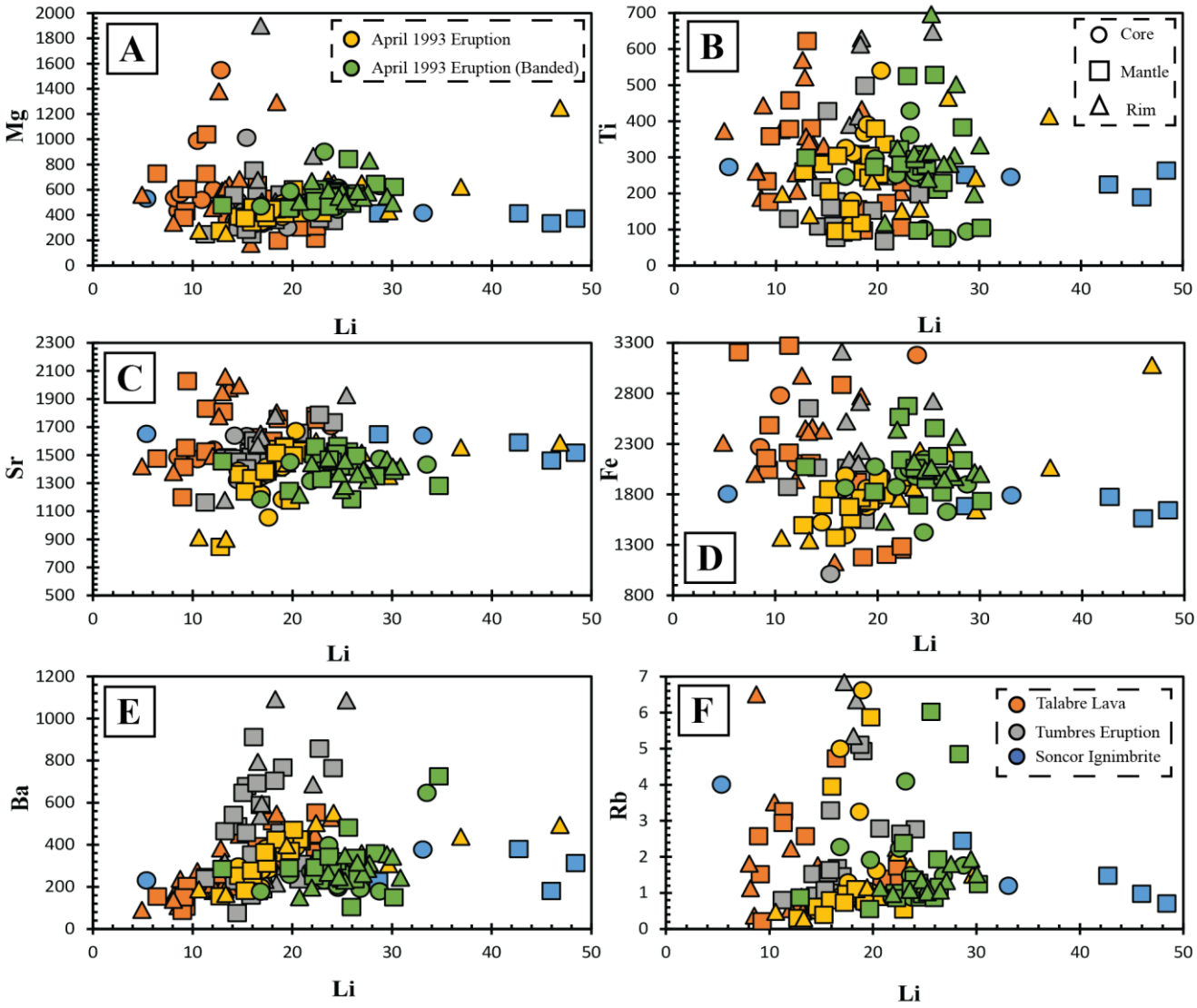

Figure 8: Trace element variation diagrams of plagioclase spot analyses for trace element compositions (ppm). Analyses are divided into core, mantle, and rim of the analyzed phenocryst.

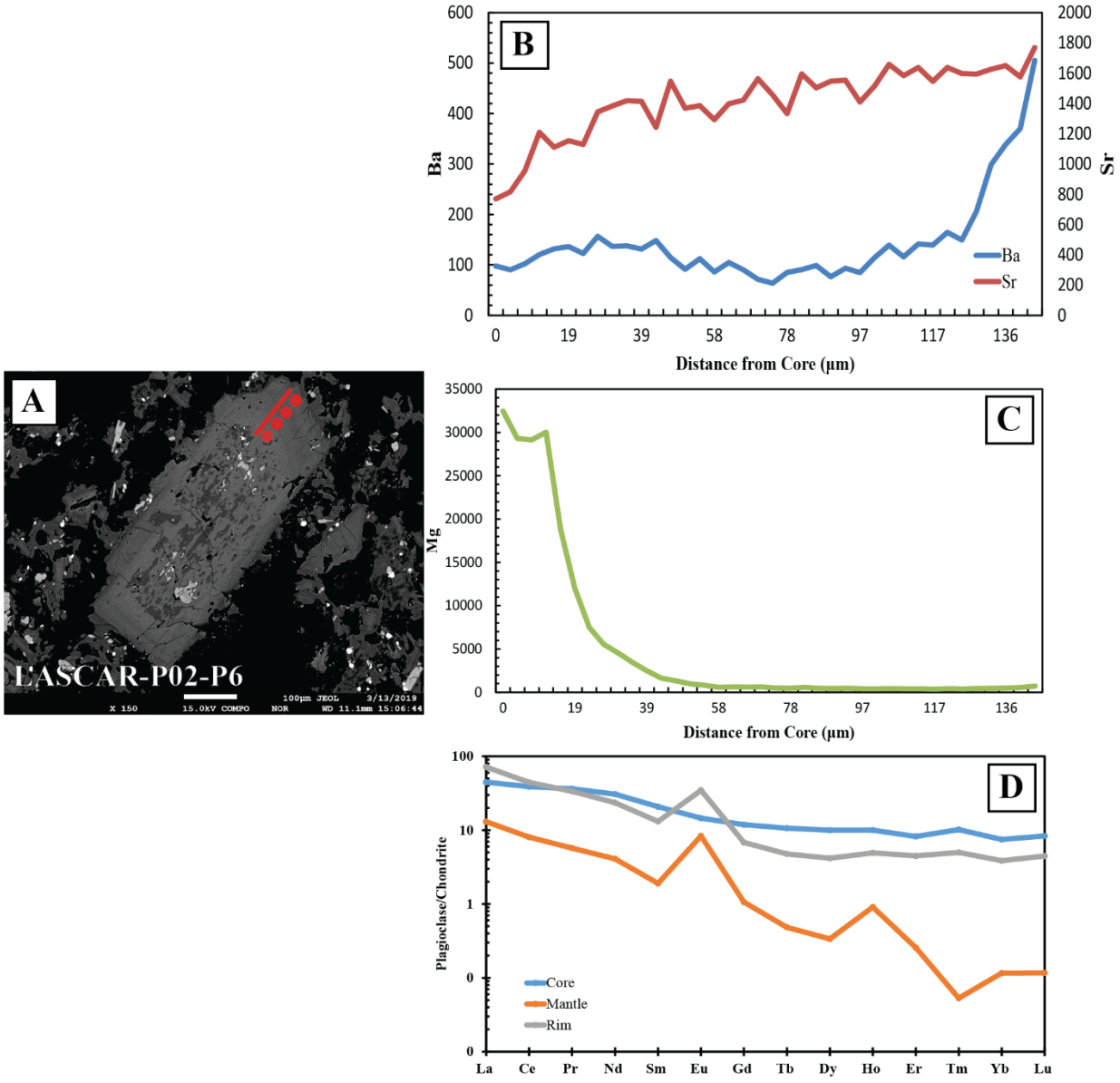

Figure 9: (A) Backscattered electron image of an analyzed plagioclase phenocryst with annotated locations of associated line transect and spot analyses. (B) Core-to-rim line transect of Sr and Ba concentrations (ppm) of the specified phenocryst. (C) Core-to-rim line transect of Mg concentrations (ppm) of the specified phenocryst. (D) Rare earth element (REE) diagram of spot analyses of the specified phenocryst, divided into representing the core, mantle, and rim of the phenocryst, normalized to chondrite (McDonough & Sun, 1995).

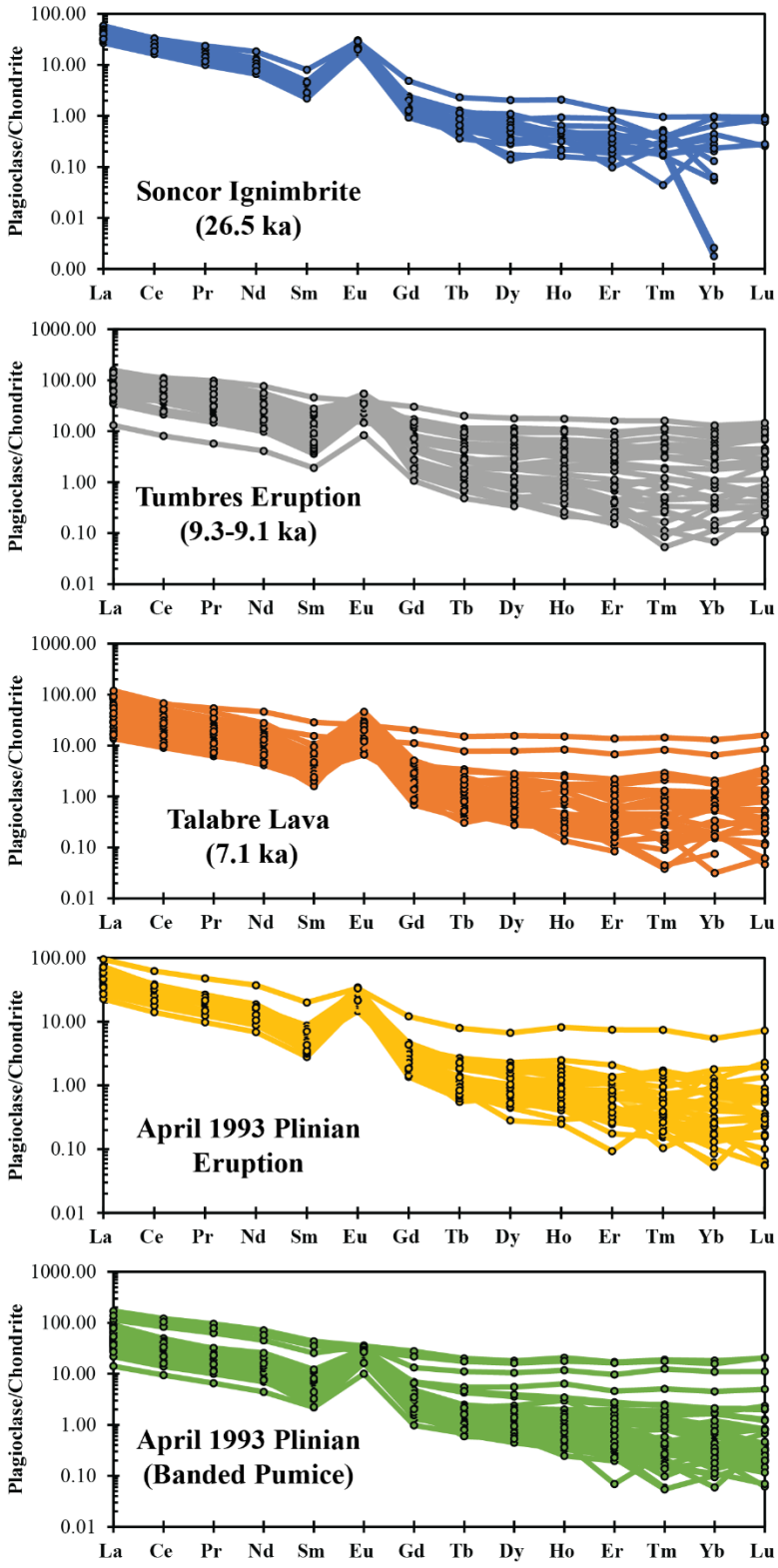

Figure 10: Rare earth element (REE) diagrams of plagioclase spot analyses, normalized to chondrite (McDonough & Sun, 1995).

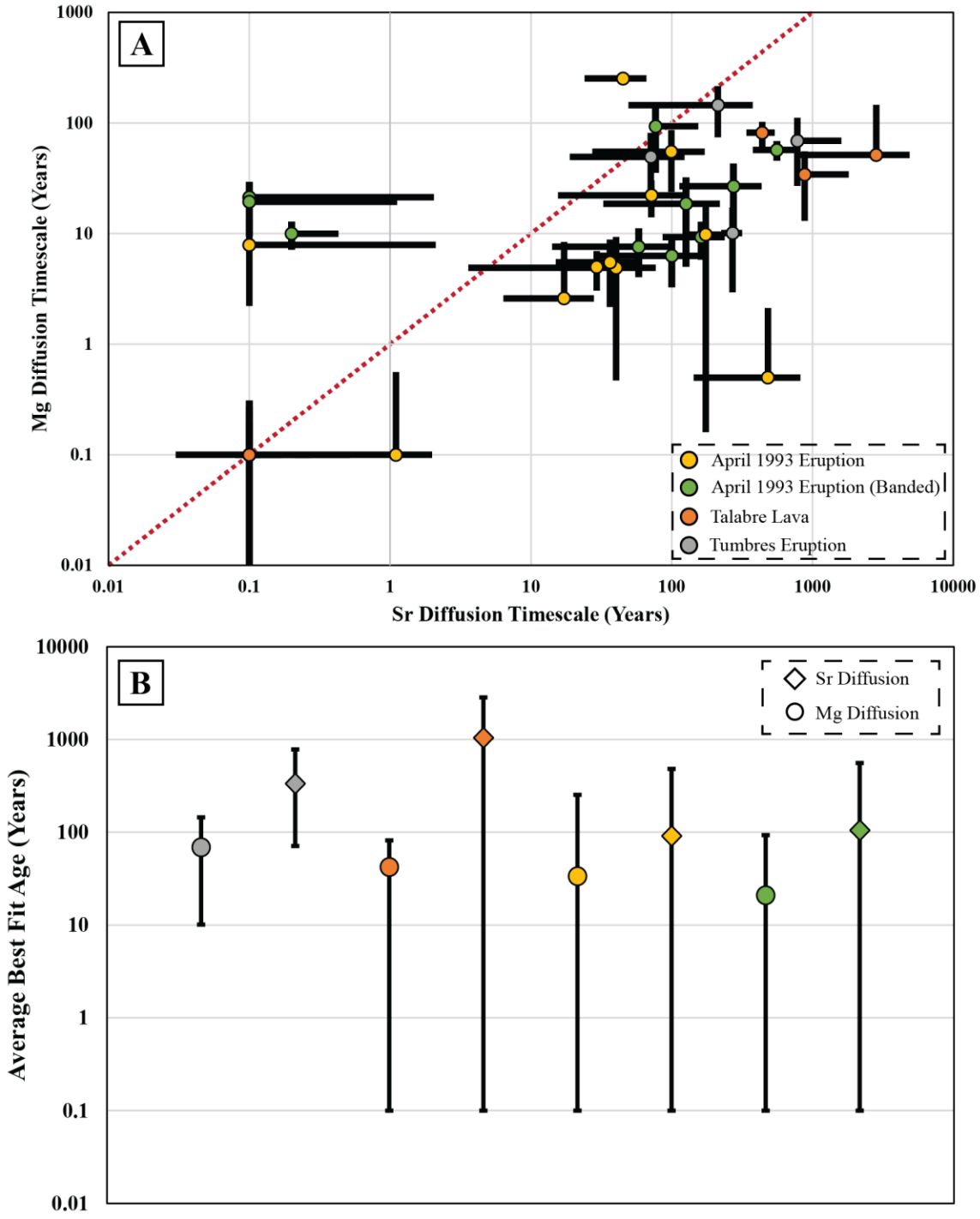

Figure 11: (A) Strontium and Mg diffusion ages for modeled phenocrysts from Láscar's stages. Python script from Lubbers *et al*. (2022), with error bars representing 2σ error. The annotated red dotted line marks a 1:1 relationship between the two modeled ages. (B) Diagram plotting the average best-fit age for each eruption, separated by element of interest. Error bars mark the oldest and youngest modeled ages for each eruption.

APPENDICES

Due to the sizes of datasets collected and utilized for the purposes of this study, complete datasets have been uploaded and are hosted at Mendeley Data. Datasets are freely available to be downloaded in their entirety. Links have been provided to access each supplimentary dataset directly.

Appendix I. Plagioclase Major Element Spot Analyses

https://data.mendeley.com/drafts/62phd293m3

Appendix II. Plagioclase Trace Element Spot Analyses

https://data.mendeley.com/drafts/62phd293m3

Appendix III. Plagioclase Trace Element Line Transects

https://data.mendeley.com/drafts/62phd293m3

Appendix IV. Sr-Mg Diffusion Models & Metadata

https://data.mendeley.com/drafts/62phd293m3